

Wright State University

CORE Scholar

[Browse all Theses and Dissertations](#)

[Theses and Dissertations](#)

2008

Automated Analysis of Metacarpal Cortical Thickness in Serial Hand Radiographs

Aarti Raheja
Wright State University

Follow this and additional works at: https://corescholar.libraries.wright.edu/etd_all



Part of the [Biomedical Engineering and Bioengineering Commons](#)

Repository Citation

Raheja, Aarti, "Automated Analysis of Metacarpal Cortical Thickness in Serial Hand Radiographs" (2008).
Browse all Theses and Dissertations. 900.
https://corescholar.libraries.wright.edu/etd_all/900

This Thesis is brought to you for free and open access by the Theses and Dissertations at CORE Scholar. It has been accepted for inclusion in Browse all Theses and Dissertations by an authorized administrator of CORE Scholar. For more information, please contact library-corescholar@wright.edu.

**AUTOMATED ANALYSIS OF METACARPAL CORTICAL
THICKNESS IN SERIAL HAND RADIOGRAPHS**

A thesis submitted in partial fulfillment
of the requirements for the degree of
Master of Science in Engineering

By

AARTI JAGDISH RAHEJA
B.E., Mumbai University, Mumbai, 2006

2008
Wright State University

WRIGHT STATE UNIVERSITY
SCHOOL OF GRADUATE STUDIES

11 December, 2008

I HEREBY RECOMMEND THAT THE THESIS PREPARED UNDER MY SUPERVISION BY Aarti Jagdish Raheja ENTITLED Automated Analysis of Metacarpal Cortical Thickness in Serial Hand Radiographs BE ACCEPTED IN PARTIAL FUFILLMENT OF THE REQUIREMENTS FOR THE DEGREE OF Master of Science in Engineering.

Julie A. Skipper, Ph.D.
Thesis Director

S. Narayanan, Ph.D.
Department Chair

Committee on Final Examination

Julie A. Skipper, Ph.D.

Dana L. Duren, Ph.D.

Thomas N. Hangartner, Ph.D.

Joseph F. Thomas Jr., Ph.D.
Dean, School of Graduate Studies

ABSTRACT

Raheja Aarti J., M.S. Egr., Department of Biomedical, Industrial and Human Factors Engineering, Wright State University, 2008. Automatic Analysis of Metacarpal Cortical Thickness in Serial Hand Radiographs.

To understand the roles of various genes that influence skeletal bone accumulation and loss, accurate measurement of bone mineralization is needed. However, it is a challenging task to accurately assess bone growth over a person's lifetime. Traditionally, manual analysis of hand radiographs has been used to quantify bone growth, but these measurements are tedious and may be impractical for a large-scale growth study. The aim of this project was to develop a tool to automate the measurement of metacarpal cortical bone thickness in standard hand-wrist radiographs of humans aged 3 months to 70+ years that would be more accurate, precise and efficient than manual radiograph analysis.

The task was divided into two parts: development of automatic analysis software and the implementation of the routines in a Graphical User Interface (GUI). The automatic analysis was to ideally execute without user intervention, but we anticipated that not all images would be successfully analyzed. The GUI, therefore, provides the interface for the user to execute the program, review results of the automated routines, make semi-automated and manual corrections, view the quantitative results and growth trend of the participant and save the results of all analyses.

The project objectives were attained. Of a test set of about 350 images from participants in a large research study, automatic analysis was successful in approximately 75% of the reasonable quality images and manual intervention allowed the remaining 25% of these images to be successfully analyzed. For images of poorer quality, including many that the Lifespan Health Research Center (LHRC) clients would not expect to be analyzed successfully, the inputs provided by the user allowed approximately 80% to be analyzed, but the remaining 20% could not be analyzed with the software.

The developed software tool provides results that are more accurate and precise than those from manual analyses. Measurement accuracy, as assessed by phantom measurements, was approximately 0.5% and interobserver and intraobserver agreement were 92.1% and 96.7%, respectively. Interobserver and intraobserver correlation values for automated analysis were 0.9674 and 0.9929, respectively, versus 0.7000 and 0.7820 for manual analysis. The automated analysis process is also approximately 87.5% more efficient than manual image analysis and automatically generates an output file containing over 160 variables of interest. The software is currently being used successfully to analyze over 17,000 images in a study of human bone growth.

TABLE OF CONTENTS

1. INTRODUCTION	1
2. BACKGROUND	3
2.1 Bone Accumulation and Bone Loss over the Lifespan.....	3
2.2 Gender-Related Differences in Bone Accumulation	4
2.3 Factors Affecting Bone Accumulation	5
2.4 Cortical Thickness	5
2.5 Region of Interest for Calculation of Cortical Index	6
2.6 Radiogrammetry	7
2.7 Blurring and Magnification in Radiographs	8
2.8 Some Previously Used Methods for Metacarpal Segmentation.....	8
2.9 Metacarpal Variables Calculated in the FLS.....	10
3. MATERIALS AND METHODS	12
3.1 Image Acquisition.....	12
3.2 Variation in the Set of Hand Radiographs	15
3.3 Automated Image Segmentation	16
3.3.1 Classifying Images Based on Histogram Analysis.....	16
3.3.2 Pre-processing of Images	20
3.3.3 Elimination of Background	22

3.3.4	Segmentation of the Metacarpal Region	23
3.3.5	Localization of the Second Metacarpal and Other Metacarpals of Interest.....	25
3.3.6	Segmentation of the Metacarpal of Interest	29
3.4	Measurement and Calculations of Various Parameters on the Metacarpals	33
3.4.1	Calculation of Total and Diaphyseal Metacarpal Lengths.....	33
3.4.2	Calculation of the Total Midshaft, Diaphyseal Midshaft and Minimum Shaft Width Locations	37
3.4.3	Location of the Endosteal and Periosteal Edges	38
3.4.4	Calculation of Medial and Lateral Cortical Thicknesses and Derived Parameters	39
3.4.5	Calculation of Blurring Correction Factor	39
3.4.6	Half Pixel Shift in the Edge Locations	44
3.5	Phantom Study to Assess Method Accuracy	45
3.5	Flowchart	49
4.	GRAPHICAL USER INTERFACE	53
4.1	Requirements of the GUI	53
4.2	Components of the GUI	53
4.2.1	Selection of the Input and Output Directory, Assessor and Wedge Type.....	55
4.2.2	Viewing the Output of the Automated Segmentation Process	57
4.2.3	Correction for Wrong Metacarpal	58
4.2.4	Correction for Wrong Approximate Length of the Metacarpal	62
4.2.5	Correction of Metacarpal Total Length	63
4.2.6	Correction of Incorrect Metacarpal Diaphyseal Length	65

4.2.7	Correction of Incorrect Cortical Thickness Measurements	66
5.	RESULTS.....	71
5.1	Edge Corrections	71
5.2	Cortical Width Plot	71
5.3	Success of Automated Analysis	75
5.4	Interobserver Agreement and Reliability	78
5.5	Intraobserver Agreement and Reliability	80
5.6	Comparison of manual versus automated measurement reliability	81
6.	DISCUSSION.....	83
6.1	Challenges in Automated Image Analysis	84
6.2	Total Cortical Width Plot	87
6.3	Other Approaches Investigated	88
6.4	Future Work	89
6.5	Conclusion.....	93
	REFERENCES.....	94

LIST OF FIGURES

Figure 2.1:	Diagrammatic representation of the metacarpal.....	6
Figure 3.1:	Image with unexposed region before and after correction.....	18
Figure 3.2:	Image with unexposed region before and after correction.....	19
Figure 3.3:	Automatic classification of a low contrast image.....	20
Figure 3.4:	Logarithmic transformation.....	21
Figure 3.5:	Segmentation of the hand from the background.....	24
Figure 3.6:	Segmentation of the metacarpal region from the hand.....	26
Figure 3.7:	Finding the second metacarpal ROI.....	28
Figure 3.8:	Obtaining the third, fourth and fifth metacarpal ROIs.....	29
Figure 3.9:	Segmentation of the metacarpal of interest.....	31
Figure 3.10:	Finding the orientation of the metacarpal.....	34
Figure 3.11:	Line profile taken along the axis of the metacarpal.....	36
Figure 3.12:	Finding the total length of the metacarpal.....	36
Figure 3.13:	Finding the diaphyseal length if it exists.....	37
Figure 3.14:	Simulation of line profile across the metacarpal.....	40
Figure 3.15:	Use of maximum curvature to locate periosteal edges.....	41

Figure 3.16:	Phantom used to find the blurring function of the system.....	42
Figure 3.17:	Finding the sigma of the gaussian blurring function.....	43
Figure 3.18:	Illustration of the half pixel shift.....	45
Figure 3.19:	Cross section of aluminum phantom used to calculate accuracy.....	46
Figure 3.20:	Radiograph of the aluminum phantom.....	47
Figure 4.1:	Layout of the GUI.....	54
Figure 4.2:	Layout of Panel A.....	56
Figure 4.3:	Layout of Panel B.....	61
Figure 4.4:	GUI for manual metacarpal selection.....	62
Figure 4.5:	Layout of Panel C.....	63
Figure 4.6:	GUI to manually adjust the approximate length.....	64
Figure 4.7:	GUI to manually adjust the total length.....	65
Figure 4.8:	GUI to manually adjust the diaphyseal length.....	66
Figure 4.9:	Layout of Panel D.....	68
Figure 4.10:	GUI for adjustment of calculated cortical thickness values.....	69
Figure 4.11:	GUI for adjusting cortical width measurements.....	70
Figure 5.1:	Illustration of the edge shift due to system blur.....	72
Figure 5.2:	Typical variation of total cortical width as a function of age.....	73
Figure 5.3:	Variation in anatomy as a function of age.....	74
Figure 5.4:	Stabilization of infant hands with spatula-like device.....	76

Figure 5.5:	Underexposed and overexposed images.....	76
Figure 5.6:	Incorrectly acquired hand images.....	77
Figure 5.7:	Results of the automated analysis routines.....	79

LIST OF TABLES

Table 3.1:	Different types of wedges imaged in hand radiographs.....	13
Table 3.2:	List of digitizers and relevant performance specifications.....	14
Table 3.3:	Phantom study results.....	48
Table 4.1:	Essential auto-analysis results variables and their description.....	57
Table 4.2:	Variables stored in the output file (Excel sheet).....	59
Table 5.1:	Corrections applied to the endosteal and periosteal edges.....	72
Table 5.2:	Measured and calculated metacarpal parameters as a function of age.....	75
Table 5.3:	Comparison of interobserver and intraobserver agreement.....	81
Table 5.4:	Comparison of interobserver and intraobserver reliability.....	82
Table 6.1:	Efficiency calculations of the automated analysis process.....	92

ACKNOWLEDGEMENT

I express my sincere gratitude toward Dr. Julie A. Skipper, under whose direction I was able to successfully complete this project and through whose encouragement I was able to realize my research potential. She has always guided me with patience through the various research obstacles and has helped me gain a better understanding of the diverse image processing concepts.

I would also like to thank Dr. Dana L. Duren, who always has been forthcoming in helping me understand the basic concept of skeletal growth and interpreting my results.

I am grateful to Dr. Thomas N. Hangartner, who recommended me for this project.

I am thankful to Ms. Kimberly Lever and Ms. Sharon Lawrence, Research Assistants, Department of Community Health, who have been using the graphical user interface tool created for this project and whose inputs have been very important in developing a more user-friendly tool.

Lastly, I would like to thank the BMIL group, who has always been very supportive and helpful during the entire process of my thesis completion.

This project was supported by grant numbers R01HD056247 and R01HD12252 from the National Institute of Child Health and Human Development of the National Institutes of Health.

DEDICATION

To my parents, Mr. Jagdish Raheja and Ms. Jaya Raheja, and my sister Ms. Pooja Raheja, for their understanding support and, most of all, love.

1. INTRODUCTION

The measurement of variation in bone geometry throughout life is an important means for monitoring bone health, of the genes affecting skeletal growth, but obtaining accurate measurement of bone mineralization, especially in children, has always been a challenge in the field of skeletal biology. Since adult bone mass is a result of genetic influence on bone accrual and bone loss, whereas child bone mass is a result of genes influencing only the bone acquisition process, it is possible to use growth measures to discriminate between genes that influence bone accumulation and genes that influence bone loss later in life. For this, it is critical that the skeletal measurement process works in both age populations. Currently, tedious manual measurements of radiographs are acquired with digital calipers. The aim of this project is to develop a tool to automate the measurement of metacarpal cortical bone thickness in standard hand-wrist radiographs that will be more accurate, precise and efficient than manual radiograph analysis.

The current project falls under the scope of the Fels Longitudinal Study (FLS), which was initiated in 1929 and is currently the world's largest and longest continuously operational serial study of growth, development and body changes throughout the human lifespan.¹ The study subjects include approximately 1,200 serial participants and approximately 1,500 nuclear and extended family members, with data spanning five

generations. Since the FLS data include serial measurements for each participant, the genetic influence on bone accrual and bone loss can be distinguished by comparing the genes affecting the bone accrual during childhood and bone accrual and loss during adulthood.

Cortical thickness measurements can be used to estimate bone mass of an individual. Bone mass represents the amount of mineralized bone in a person and is generally expressed in units of g/cm^2 . Bone mass accumulates most rapidly during childhood and gradually peaks in early adulthood.^{1,2} Peak bone mass is the amount of bone present at the end of skeletal maturation. In later life, bone loss occurs as a result of an imbalance between rates of bone formation and resorption during bone remodeling.³ All of these changes can be tracked by looking at the serial data from the FLS participants.

2. BACKGROUND

2.1 Bone Accumulation and Bone Loss over the Lifespan

Bone mass accumulation begins at the onset of endochondral ossification which, for some bones, occurs during the fetal stage. There is a marked increase in bone mass accumulation during puberty, with peak bone mass attained between the ages of 20 and 30 years.² The process of bone loss typically starts in the fifth decade for both males and females.⁴

Cortical bone mass accumulation and loss take place at two bone surfaces in the diaphysis of any long bone: the periosteal surface and the endosteal surface (Figure 1.1a). At the periosteal surface, the changes are positive since there is periosteal apposition rather than resorption.⁴ The early periosteal apposition rate is very high and is followed by a moderate rate of increase until puberty. There is a rapid increase in the periosteal apposition during adolescence, after which time the periosteal apposition continues at a slower rate and progresses until about the age of eighty years.⁴

The changes at the endosteal surface are more complex. Three phases occur in the endosteal growth cycle: 1) a resorption phase (birth to approximately age 20 years), wherein resorptive losses are higher in males than in females; 2) an apposition phase (approximately age 20 to age 40 years), which takes place after the periosteal apposition

rate spurt during adolescence and again occurs at a greater rate in males versus females; and 3) another resorption phase (age 40 years until the end of life), which is the primary cause of bone loss in adults due to the disproportionate ratio of endosteal resorption to periosteal apposition.⁴

Although cortical bone represents the majority of skeletal bone mass, trabecular bone is also of clinical interest. Trabecular bone is found near the ends of long bones at joint surfaces and within the vertebrae.⁵ Due to its large surface-to-volume ratio and the fact that the trabeculae are in direct contact with bone marrow, trabecular bone exhibits high metabolic activity (bone turnover) and responds more quickly to environmental and hormonal changes.⁶ In this project, since measurements are taken in the midshaft region of the metacarpal, cortical measurements are of interest.

2.2 Gender-Related Differences in Bone Accumulation

Males and females have a more or less similar pattern for bone deposition until the onset of puberty.³ At the early stages of puberty, bone accumulation in females is markedly increased over that in males. However, the bone mass is higher at the end of puberty in males due to the longer duration and increased rate of periosteal apposition, which yields a larger periosteal diameter throughout the lifespan.⁴ Conversely, adolescent endosteal apposition is higher in females than in males, resulting in a narrower medullar cavity in females. The rate of bone loss is higher in females than in males but is due to lower periosteal bone formation in females and not a result of increased endosteal resorption.⁷ This is also seen in post-menopausal females where there are decreased levels of estrogen which, in turn, inhibit periosteal bone formation due to a decrease in osteoblast (bone forming cells) activity.⁷

2.3 Factors Affecting Bone Accumulation

Bone accumulation is the product of sexual maturation and genetic and environmental factors.⁸ Genetic factors regulate how efficiently the body utilizes its nutrients during bone remodeling.⁹ Genetic factors have physiological and pathological effects on bone mass accumulation. For example, some genetic disorders such as osteogenesis imperfecta (OI), which is a congenital disorder, lead to low bone mass and bone fragility due to malfunctions in the production of collagen.¹⁰ Environmental factors, including nutritional intake and exercise, can have either a positive or negative influence on bone mass accumulation.⁸ For example, a protein-deficient diet delays the adolescent growth spurt and yields a diminished adult periosteal diameter. Bone loading during exercise increases bone mass, whereas physical immobilization results in loss of bone.

2.4 Cortical Thickness

An estimate of a person's bone mass can be calculated by directly measuring the cortical thickness of the metacarpals. As in other long bones, the shafts of the metacarpals are comprised of approximately 80-90% cortical bone and 10-20% trabecular bone.¹¹ In a cylindrical segment of a long bone, the net cortical thickness TC is equal to the periosteal diameter TD minus the endosteal (medullary cavity) diameter MD (Figure 1.1b). Cortical thickness increases from early infancy until approximately the fourth decade in life. During adolescence, the rate of increase in cortical thickness is higher in females but has a longer duration in males, leading to a greater cortical thickness in males.⁴

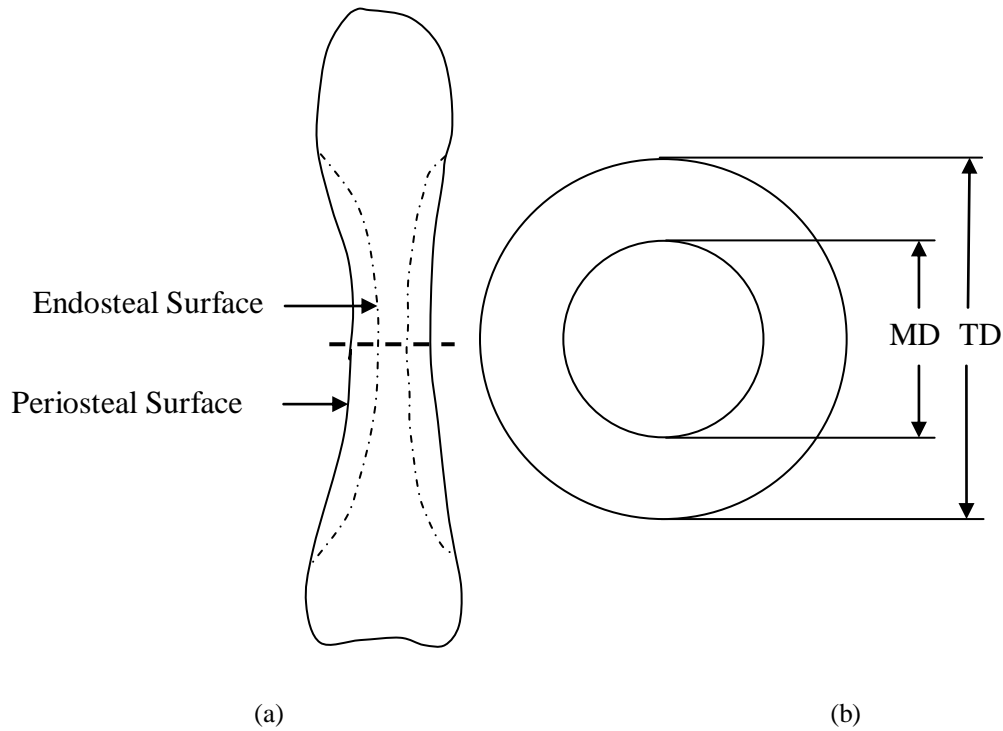


Figure 1.1. Diagrammatic representation of the metacarpal, showing a) the periosteal and endosteal surfaces where bone mass accumulation and loss predominantly occur during growth stages and b) the cross-section of the bone (at the location indicated by the dashed horizontal line in (a)) with the dimensions of total periosteal diameter TD and medullary cavity diameter MD displayed. The net total cortical thickness TC is equal to $TD - MD$.

2.5 Region of Interest for Calculation of Cortical Index

The metacarpals of the non-dominant hand were selected as regions of interest (ROI) in this study. Metacarpal measurements are common in radiogrammetry studies due to easy accessibility for imaging and the fact that the cortex of the metacarpal typically represents 90% of that bone's bone mineral content (BMC).¹² In fact, the metacarpal cortical index (MCI) was used as an index of osteoporosis before dual x-ray absorptiometry (DXA) technology was developed. MCI is usually expressed as a ratio of the total cortical thickness (medial and lateral) normalized by the outer bone diameter of the same bone at the same location.¹³

2.6 Radiogrammetry

Radiogrammetry has been used since the 1960's to calculate bone mass from radiographs.¹³ By measuring the metacarpal endosteal and periosteal diameters from hand radiographs,¹⁴ changes in periosteal apposition and endosteal resorption can be assessed. In conventional radiogrammetry, geometric dimensions are measured by an observer using a measuring instrument (e.g., calipers). Radiogrammetry is different from other methods for bone mass measurements as it returns the geometric dimensions, rather than the material density, of the bone. Accordingly, it is less sensitive to beam hardening effects and soft-tissue thickness.¹⁵ Since radiogrammetry involves measurement from radiographs that may have been acquired years prior, but are still available, it can be used in large populations or for serial studies to determine changes in bone thicknesses throughout an individual's life span.

With advances in computer radiography and image processing methods, more precise methods have become available to determine bone mass from digital radiographs. The newer method is known as digital X-ray radiogrammetry (DXR) and involves computer analysis of digitized radiographs. The major advantage of DXR over conventional radiogrammetry is observer independence because (in theory) no observer measurements are necessary.¹² The accuracy of digital radiogrammetry can be improved by using film digitizers or sensors with high spatial resolution, and DXR is far more accurate than conventional radiogrammetry since the digitized pixel size is much smaller than the difference the eye can perceive during measurement with the digital calipers.

2.7 Blurring and Magnification in Radiographs

Blurring of an object on an x-ray film is a common characteristic in radiographs. Image unsharpness due to patient motion is one blur artifact that cannot be corrected for systematically. However, another source of blurring is the finite size of the x-ray focal spot, which results in a region of partial irradiation surrounding the object.¹⁶ Since the focal spot is not a point source, it behaves as if it were composed of many x-ray point sources, each forming its own image of the object. The edges of these images will not be at the same point on the film, leading to an ill-defined edge or penumbra around the object. This geometric unsharpness, or edge gradient, appears visually as blurring. Since blurring primarily depends on the size of the x-ray focal spot, it is an imaging device property and varies with the imaging system. For accurate quantitative analysis of bone geometry, a blurring correction is required.

Object magnification also affects the apparent dimensions of radiographed objects. The amount of magnification M is affected by both the source-to-film distance D_{sf} and the source-to-object distance D_{so} as follows:

$$M = \frac{D_{sf}}{D_{so}} . \quad [1]$$

2.8 Some Previously Used Methods for Metacarpal Segmentation

Commercial instruments are available for radiogrammetric measurements of bone. For example, Pronosco's X-Posure SystemTM (Sectra Pronosco A/S, Vedbaek, Denmark) automatically calculates the MCI from hand radiographs.¹⁷ This system's software uses an active shape model (ASM) to find the diaphyses of the middle three metacarpals, and then automatically selects the region around the minimum shaft width. Within this region,

the endosteal (inner) edges are determined from the maximum grayscale-intensity values along each row's line profile and the periosteal (outer) edges, are found from the sets of adjacent points having the maximum gradient.¹⁷

Other researchers have worked on methods for hand radiograph analysis. Sotoca et al. used point distribution models (PDM) and ASMs for automatic segmentation of hand bones in digitized hand radiographs.¹⁸ PDMs are statistical models that change shape depending on allowable deformation as determined by analysis of a training set of images. The software is fine tuned with the help of a training set by allowing variation in the possible model deformations. This variation in the model to construct the desired shape is called the ASM. The number of points for the model differed according to the bone being segmented, which was manually selected by choosing a seed point inside the bone. Once the contours of the bone are successfully found, the average grayscale value of the region is reported.

Garcia et al. developed a fully automatic algorithm for the segmentation of phalanges in hand radiographs.¹⁹ Their method was divided in two parts: finding the seed point for the active contours (snakes), then using the snakes to achieve segmentation. They first separated the hand silhouette from the background by applying a threshold value based on local statistics. The skeleton of the hand was then generated from the binary hand image and the branches of the skeleton were used to find seed points inside the phalanges. Subsequently, the seed points were used to define candidate bone contours. The internal and external energies due to the gradient of the image, in concert with the adaptive snake algorithm around the bone of interest, were used to create the final bone contour.

2.9 Metacarpal Variables Calculated in the FLS

In this section, the major metacarpal variables of interest in the FLS will be defined. Historically, the variables have been collected manually along the metacarpal.¹ Additional values were derived from the above measurements. Over the past five years or so, measurements have been taken with digital calipers and fed directly into a PC.

For each of the metacarpals of interest (second through fifth), the total metacarpal length and diaphyseal metacarpal length measurements were first acquired. In the cases wherein diaphyseal/epiphyseal fusion was complete, the diaphyseal length was not determined. These values were then used to determine three positions on the metacarpal: midshaft of total length, midshaft of diaphyseal length and position of minimum shaft width. At each of these three positions, four values were measured:

1. Total Diameter *TD*: The periosteal diameter
2. Medullary Diameter *MD*: The diameter of the medullary cavity, corresponding to the distance between each endosteal surface
3. Medial Cortex Thickness *MC*: The distance between the periosteal and endosteal edges on the medial side
4. Lateral Cortex Thickness *LC*: The distance between the periosteal and endosteal edges on the lateral side.

Four additional values were derived from the measured variables:

5. Total Cortex *TC*: The sum of the medial and the lateral cortical thicknesses, given by

$$TC = MC + LC \quad [2]$$

6. Cortical Index *CI*: The ratio of total cortex to bone diameter, given by

$$CI = \frac{MC+LC}{TD} \quad [3]$$

7. Polar Moment of Inertia *TJ*: A bending strength indicator, given by

$$TJ = \frac{\pi(TD-MD)}{32} \quad [4]$$

8. Polar Section Modulus *TZP*: A torsional strength indicator, given by

$$TZP = \frac{TJ}{TD}. \quad [5]$$

3. MATERIALS AND METHODS

3.1 Image Acquisition

Over 17,000 hand radiographs (typically between 20-45 images per participant) are to be analyzed in this FLS effort under the direction of Dr. Dana Duren. The visit schedule for each FLS participant follows: from birth to age one year, data are collected every three months; from the age of one year to 18 years, data are collected every six months; from 18 years onward there is no fixed time interval between visits. Since the FLS originated in 1929, several x-ray tubes have been used to acquire the hand radiographs. The imaging protocol has changed slightly over the years: the current hand radiograph acquisition protocol parameters are: 50 kVp, 12 mA, 0.1 s at a source-to-film distance of 40 in. All radiographs were taken in the posteroanterior (PA) view. For calibration purposes, a reference aluminum wedge was included in some of the radiographs. The different types of wedges included in the radiographs are listed in Table 3.1.

The film size used during this study was not uniform; the smallest film size was 3"x5", whereas the typical and largest film size was 8"x10". In some cases, when the quality of the acquired radiograph was questionable, a second radiograph was acquired at the same visit and both films were available in the image database.

Table 3.1. Different types of wedges imaged on hand-wrist radiographs over the years in the FLS. A wedge was not present in some radiographs. Not all wedges are included here, because some wedges are not cataloged and are labeled as ‘Other.’

Wedge Types	
Double	Small Step
Large Step	Small Step and Slope
Medium Step	Small Step and Double
Pyramid	Medium Step and Slope
Slope	Ruler

Comparison of Digitizers

One of the first steps was to specify an appropriate film digitizer for this project. Film digitization is required for the automatic analysis routines and also provides permanent archiving of the acquired radiographs. Of interest was a digitizer that would provide both high grayscale resolution and high spatial resolution. A high spatial resolution was required for accurately localizing edges of the metacarpals and a high grayscale resolution aides in edge definition and permits later analysis of bone mineral density. Several digitizers were considered; their specifications are compared in Table 6.1. Based on cost and performance specifications, the VIDAR DosimetryPRO Advantage[®] film digitizer (VIDAR Systems Corporation, Herndon, VA) was selected. This digitizer provides a nominal 16-bit grayscale resolution and 300 dpi (85 μ m pixel size) spatial resolution.

The typical resultant digitized images were approximately 2880 x 2220 pixels. During the digitization process, the following file naming scheme was adopted: each filename consisted of 20 or 22 characters. The first eight characters identified the participant

Table 3.2: Several film digitizers were considered for purchase by the Lifespan Health Research Center (LHRC) researchers. This table provides a listing of the digitizers and relevant performance specifications of each instrument.

Manufacturer	Model	Grayscale Resolution	Spatial Resolution	Optical Density Range	Film Processing Speed	Max Films/Batch	Cost	Notes
Kodak	Industrex LS85	12 bit	73 μm	0.03-3.85	88 s at "highest resolution"	N/A	\$57,900	Includes PC system with monitor
Radlink Golbar Radiography	Laser Pro 16	16 bit	166 μm	0-4.0	13 s (1K) 26 s (2K) 39 s (3K)	8	\$15,500	\$14,000 without Autoloader
Vidar Systems	Dosimetry Pro Advantage	16 bit	89 μm	0.0-4.0	24 s (4Kx5K)	25	\$20,905	Speciality device sold only to cancer centers
Vidar Systems	Sierra Plus	12 bit	85 μm	0.02 - 3.6	82 s (4Kx5K)	N/A	\$10,995	No multifeed option
Vidar Systems	Diagnostic Pro Advantage	12 bit	85 μm	0.05-4.0	40 s (4Kx5K)	25	Single feed-\$12,000 Multifeed-\$19,945	-
GE	FS50/FS50B	12 bit	50 μm	0.05-4.0	7 s at 200um 120 s at 50um	N/A	\$75,750	Includes workstation and monitor
GE	Lumiscan 75	12 bit	100 μm	0.3-4.1	~ 31 s	6	-	-
GE	Lumiscan 20	12 bit	175 μm	0.3-3.8	~ 13 s	6	-	-
Howtek	Fulcrum	16 bit	42.3 μm	0.0-4.4	23 s	N/A	\$39,900	-

number, which was present on the radiograph. The next eight characters indicated the visit date in yyymmdd format and the last four characters were the word 'HAND' to identify the body part. When two radiographs were acquired during a single visit, the 21st character was entered as 'A' for the first radiograph or 'B' for the second radiograph; the radiograph most suited for analysis was indicated by a '1' in the 22nd character position (a '2' was entered in this position for the less suitable film).

3.2 Variation in the Set of Hand Radiographs

Since the FLS participants were involved in a longitudinal study, their age at the time of image acquisition ranges from three months to sixty years. However, the acquisition parameters did not change based on the subject's age. Consequently, most infant films were overexposed and of poor contrast due to low amount of mineralized bone. Additionally, the radiographs acquired at the beginning of the study have been in storage for over seventy years and are beginning to deteriorate. Copies of some original films were made in order to preserve the information. The copies were made onto films that were larger than the originals, and these films have a substantial unexposed border. Both of these issues impact automated segmentation routines and are addressed in the following sections.

The project is broadly divided into three parts:

1. Automated segmentation of the desired metacarpal
2. Measurement/calculation of required metacarpal analysis parameters

3. Construction of a graphical user interface (GUI) to the software routines. The GUI provides functionality for a) automatic analysis, b) results review and manual corrections by user, c) storage of analysis results and d) post-review of accepted analyses.

A flowchart summarizing the algorithmic steps for segmenting and measuring the metacarpal is provided in Section 3.5.

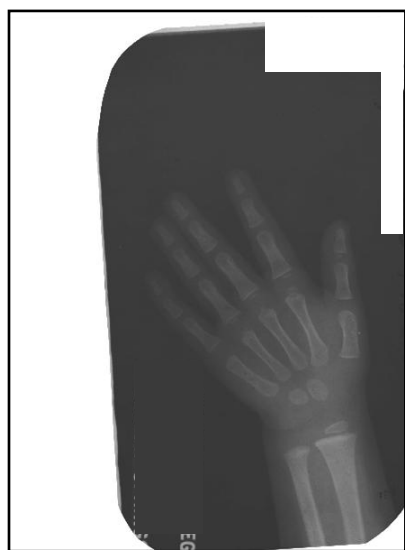
3.3 Automated Image Segmentation

An algorithm was developed to automatically segment the metacarpal of interest from the hand radiograph. This task was achieved through the following steps: classifying images based on histogram analysis, pre-processing of images, elimination of extraneous background objects, segmentation of the general metacarpal region, localization of the metacarpal of interest and segmentation of the metacarpal of interest.

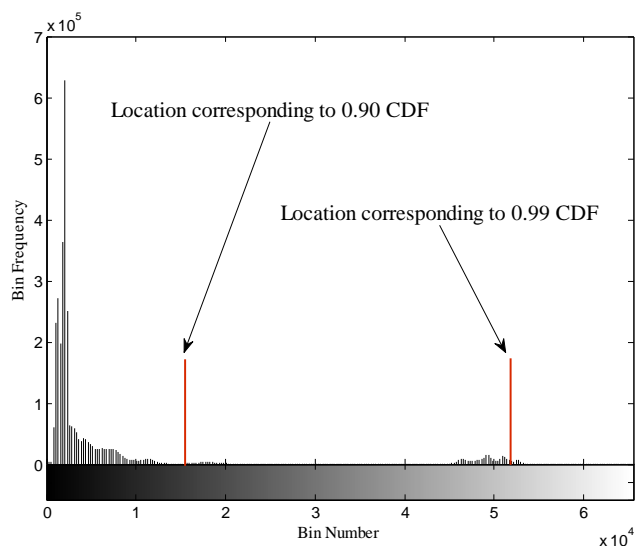
3.3.1 Classifying Images Based on Histogram Analysis

Given the variation in the images, each image may or may not require particular pre-processing steps. To automatically determine which steps to apply, images were analyzed by evaluating the image histogram, which represents the distribution of the grayscale values across the dynamic range of the image. The dynamic range of the image is dictated by the imager's bit depth; here, digitized 16-bit images yield grayscale values ranging from 0 to 65,535. Histogram analysis allowed images to be classified based on the need for two distinct pre-processing steps: removal of unexposed areas and correction for overexposure.

Images with unexposed areas (Figure 3.1a) exhibit histograms with a substantial number of pixels in a narrow region in the upper dynamic range that are not contiguous with the remaining histogram values (Figure 3.1b). These values needed to be suppressed in the image to avoid biasing the threshold value required in subsequent hand segmentation steps. To determine if an image contained an unexposed region, the cumulative distribution function (CDF) of the histogram was used. Grayscale cutoffs that correspond to 90% and 99% of the CDF were calculated. The difference between these two values was higher in images with unexposed regions as compared to uniformly exposed images. Through trial and error, we found that a difference value greater than 30,000 indicates the presence of unexposed regions (Figure 3.1), and all the pixels lying in the region (0.99 CDF-10,000) were classified as unexposed in this case. A second condition was also necessary, since some images had a very large number of unexposed pixels, which yielded 90% and 99% CDF cutoffs at high grayscale values. In this case, the presence of unexposed regions was indicated if the difference value was greater than 10,000 and the 99% value was greater than 50,000 (Figure 3.2). All pixels lying in the region (0.90 CDF-10,000) were classified as unexposed in this case. To automatically detect overexposed images, the grayscale cutoff corresponding to 95% of the histogram CDF was computed. If this value was below 10,000 (approximately 15% of the total dynamic range), the image was classified as having poor contrast (Figure 3.3a). Note that for images containing an unexposed region, the 95% value is calculated after eliminating the unexposed regions from the image.



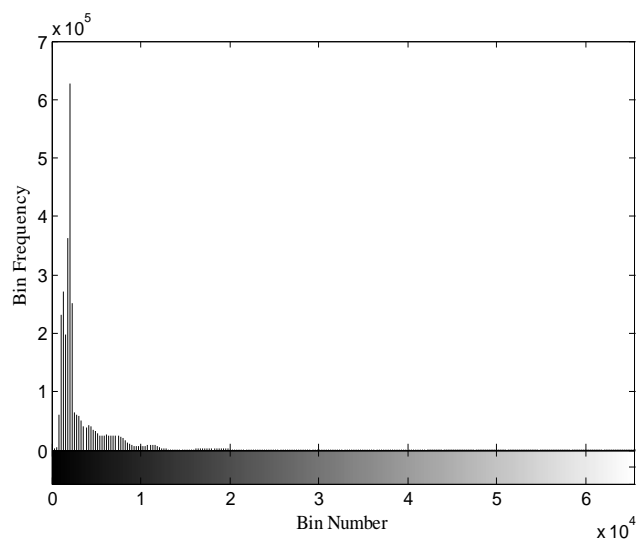
(a)



(b)

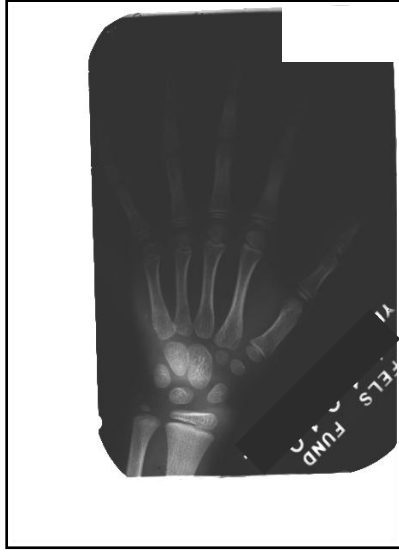


(c)

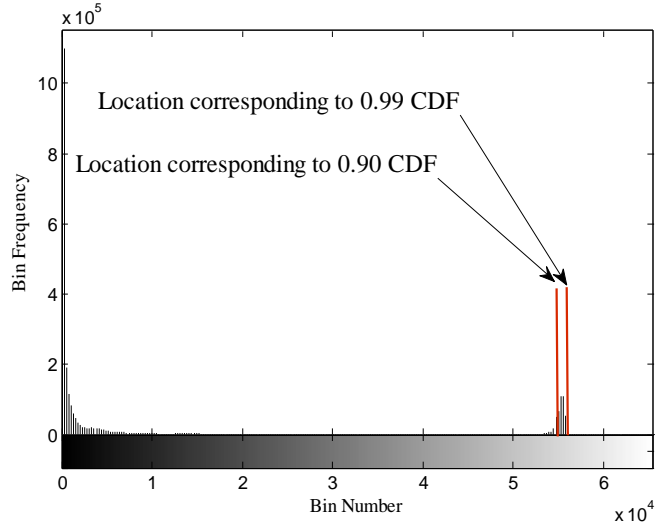


(d)

Figure 3.1. a) Image containing unexposed region after film duplication, along with its b) histogram, showing a corresponding region in the higher dynamic range unrelated to the rest of the histogram. The grayscale locations corresponding to 90% and 99% of the cumulative distribution function (CDF) of the histogram are displayed. Since there is a large difference between these two grayscale values, the given image is classified as having an unexposed area, and subsequent pre-processing steps are invoked to eliminate that area. c) The resultant image and d) its histogram after pre-processing, showing that the unexposed region has been suppressed by setting all pixels with grayscale values greater than $(0.99 \text{ CDF} - 10,000)$ to 0.



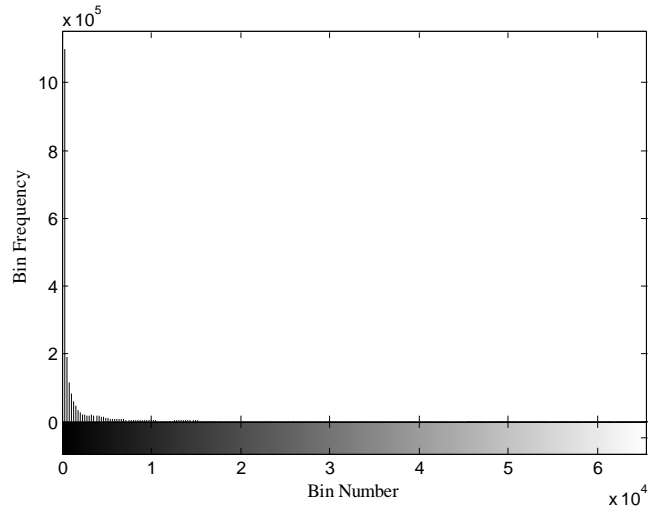
(a)



(b)



(c)



(d)

Figure 3.2. a) Image containing an unexposed region along with its b) histogram showing the unwanted group of unexposed pixels. In contrast to the case presented in Figure 3.1, here the difference between the grayscale cutoff values is fairly small, and the second conditional statement is invoked. Since the 0.99 CDF grayscale value is large ($> 50,000$), this image is classified as having an unexposed area. After preprocessing, all pixels greater than $(0.90 \text{ CDF} - 10,000)$ are set to zero. c) The processed image and d) its histogram exhibit no unexposed areas.

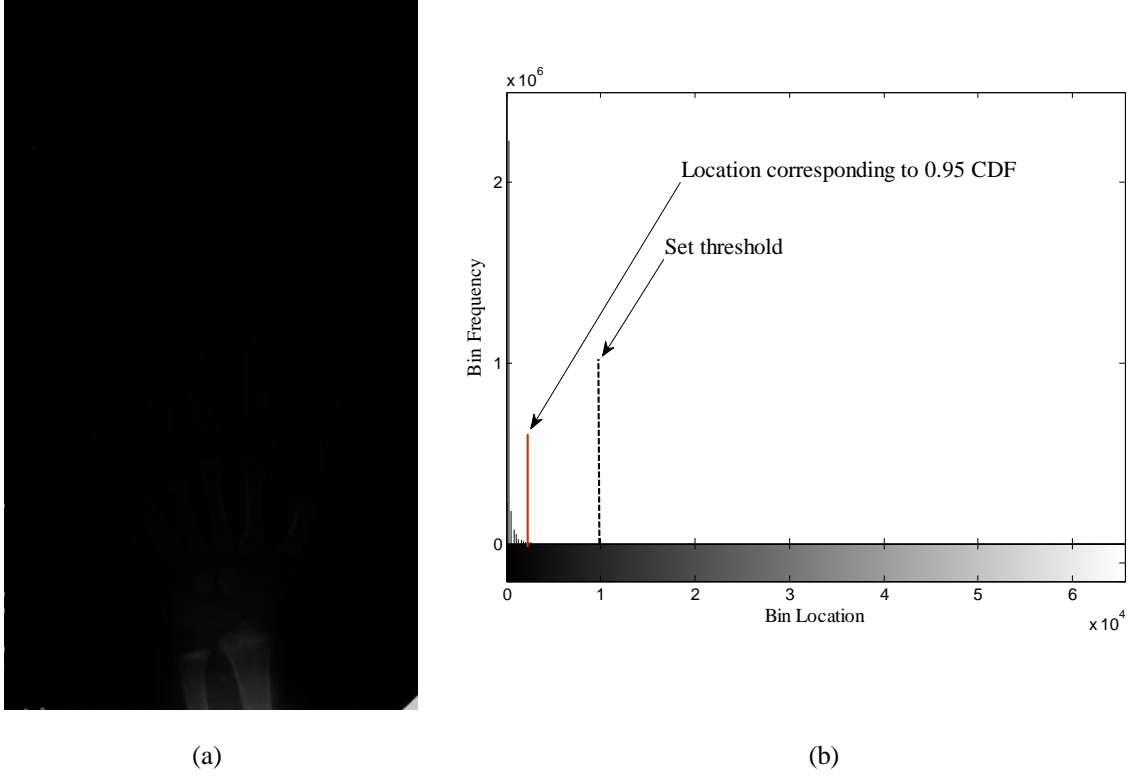


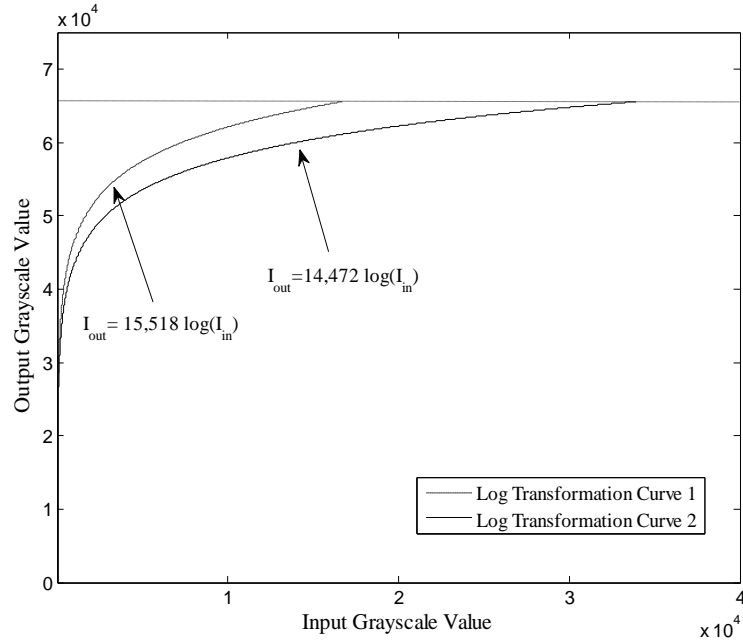
Figure 3.3. a) A given image is automatically classified as having low contrast (usually due to overexposure), if the grayscale value corresponding to 0.95 CDF lies below the set threshold of 10,000 as observed in b) its corresponding histogram.

3.3.2 Pre-Processing of Images

To suppress unexposed image regions, the pixels having grayscale values within the defined range were set to zero (black). Next, an image-dependent logarithmic transformation was applied to all images (Equation 6). Further, clipping is avoided through the use of an appropriate scaling factor as follows:

$$I_{out} = c \log(I_{in}), \quad [6]$$

where I_{out} is the output pixel value after the log transformation is applied to I_{in} , the input



(a)



(b)



(c)

Figure 3.4. a) An image-specific logarithmic transformation is applied to each image to stretch the dynamic range occupied by its histogram and to find the desired threshold value to segment the hand from the background. The constant in Equation 1 is selected such that, after applying the log transform, the histogram of the image occupies the entire dynamic range. Two such curves are plotted, showing that a narrow input grayscale range is remapped to cover a wider output grayscale range. b) Low contrast image before and c) after application of its unique logarithmic transform.

pixel value and c is the constant that was selected to yield a maximum output grayscale value of 65,536 (meaning that the transformed image values occupy the entire dynamic range). The constant c is, therefore, defined as

$$c = \frac{2^n}{\log(I_{\max})}, \quad [7]$$

where n is the bit depth resolution and I_{\max} is the maximum intensity value in the input image.

This remapped the original range of grayscale values onto a wider range of output grayscale values (Figure 3.4),²⁰ which generally improves image contrast and aids in later finding an appropriate segmentation threshold value. This process worked well for both properly exposed and overexposed images. For hand-wrist radiographs, the image grayscale values lie in the lower portion of the dynamic range and so these values are stretched rather than compressed as a result of the logarithmic transformation.

3.3.3 Elimination of Background

Next, the hand was segmented from the background using a modified version of Matlab's *graythresh* function, which applies Otsu's method to select an optimal threshold for classifying image pixels into distinct classes.²¹ There are a number of pixels in the image having a grayscale value equal to zero, particularly in the cases wherein unexposed regions were set to OFF during pre-processing. These pixels should not contribute to the selection of a global threshold value, and thus the value at this position of the histogram (i.e., the number of pixels in that bin) was reset to zero. In Otsu's method, an optimum threshold is determined to minimize the within class variances of the background and

foreground pixels.²¹ Otsu's method is most accurate when the variance within each class is inherently low, a condition that is met in this application. The Otsu-suggested threshold is intentionally lowered in all cases to avoid losing hand pixels. For overexposed images, the returned threshold value was adjusted to a value 15% lower than the Otsu-suggested threshold, as opposed to a 10% lower value for good contrast images, to account for the higher incidence of low grayscale values. To verify that the selected threshold was appropriate, the total number of ON pixels in selected image regions was determined. If too many ON pixels existed, then the threshold was increased by 10%. This process was continued iteratively until the number of ON pixels met the expectations of an appropriately segmented hand image, with only the pixels within the hand turned ON.

In our application, the original image (Figure 3.5a) was to be divided into two regions: hand pixels and background pixels; we wished to turn the hand pixels ON (white) and the background pixels OFF (black) (Figure 3.5b). However, in some images, background objects outside the hand (such as patient identification letters, the calibration wedge, etc.) had similar grayscale values as the hand and were turned ON. Since these background objects were unnecessary in subsequent analysis steps, we wanted to set these pixels OFF. As the hand was the largest object in the image, it was easily separated from the background objects by counting the pixels in each object and selecting the largest object to turn ON (Figure 3.5c).

3.3.4 Segmentation of the Metacarpal Region

Following hand segmentation, the next task was to identify the metacarpal region. This was achieved in two steps.

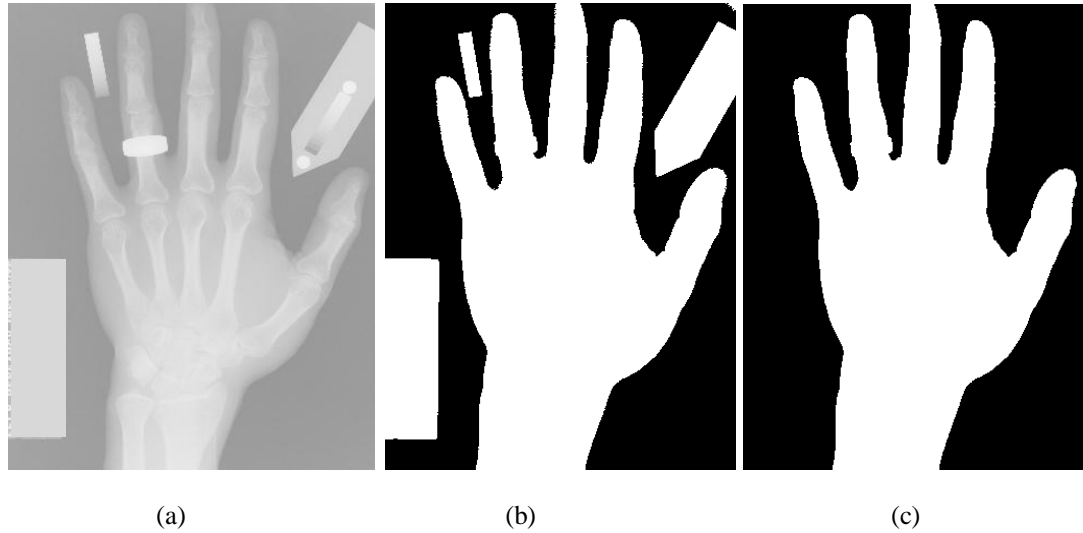


Figure 3.5. To segment the hand from the background, a) the input image is thresholded using Otsu's method to obtain a b) binary image. Since the binary image also contains unwanted objects, such as the patient identification marker and calibration wedge, selection of only the largest object in (b) results in c) a binary image of the hand.

3.3.4.1 Identification of the Phalanges Region

Along each row of the binary hand image, the number of zero crossings was counted. A zero crossing occurred whenever there was a transition from an ON (grayscale value = 1) pixel to an OFF (grayscale value = 0) pixel or vice-versa. Consequently, the number of zero crossings decreases when the fingers transition to the palm region as the rows progress distally-to-proximally along the hand. Since the metacarpals are located just below the phalanges, an upper threshold for cropping the metacarpal region was selected when the numbers of zero crossings fall below a threshold of six. This threshold works best because, although there are two zero crossings for each finger (not counting the thumb due to its orientation), in some cases the entire hand is rotated and fewer than eight zero crossings exist even in the phalanges region. Subsequently, a fixed number of rows

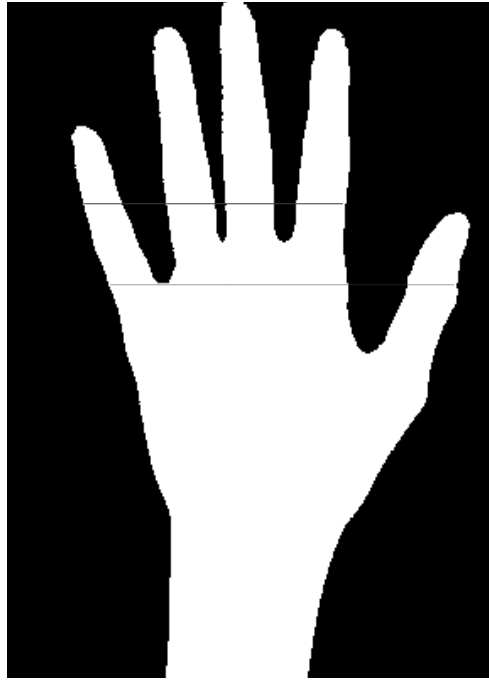
were added as a buffer to prevent inadvertent cropping of the distal metacarpal regions (Figure 3.6a).

3.3.4.2 Separating the Carpal and Metacarpal Regions

After the first step, the binary image includes regions of the metacarpals, carpals and proximal radius and ulna (Figure 3.6b). After masking the original image with this binary mask, the resultant image was again thresholded using Otsu's method to segment bone from soft tissue (Figure 3.6c). Next, a similar zero-crossing method was again applied to obtain the metacarpal region. When, working proximally-to-distally, the number of zero crossings in an image row exceeded four (determined by trial and error), the proximal limit of the metacarpal region was reached. This information was subsequently used to extract the metacarpal image of interest (Figure 3.6d).

3.3.5 Localization of the Second Metacarpal and Other Metacarpals of Interest

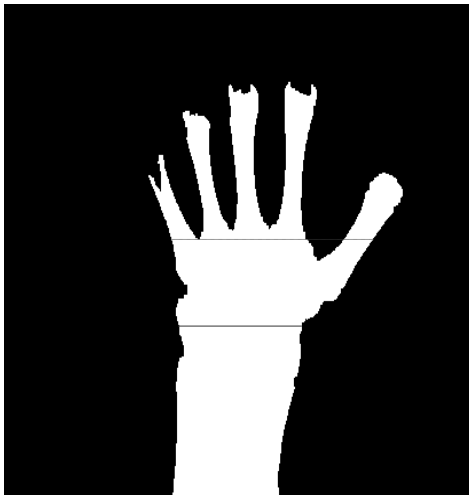
A Medial Axis Transform (MAT) was used to find the specific region around the second metacarpal. This transform is based on a Euclidean Distance Map (EDM), which converts a binary image into a grayscale image, wherein each foreground pixel in the input binary image is assigned a grayscale value based on its Euclidean distance from the nearest background pixel. The result is that pixels closer to the object's edges will have lower grayscale values than pixels closer the object's centers.²² As a result, pixels equidistant from two background pixels will form a ridge of locally bright values in the EDM. Generation of these ridges in an object's image constitutes the MAT. Since the success of the MAT depends on the quality of the input binary image, a two-step process for



(a)



(b)



(c)



(d)

Fig 3.6. To segment the metacarpal region from the hand, we first find a) the location (dotted line) on the binary image where, working distally-to-proximally, the number of zero crossings first falls below six. By adding a constant number of buffer rows, the image is cropped at the position of the solid line to remove the phalanges. After cropping the original image at the position of the dotted line, the b) resulting grayscale image is again subjected to Otsu's method to find a new threshold for binarization. c) In the resultant binary image, a new position (dotted line) is found where, working proximally-to-distally, the number of zero crossings first exceeds four. After adding a constant number of buffer rows (ending at the solid line), the image (b) is re-cropped at the position of the solid line in (c) to remove the regions of the radius, ulna and some carpals to yield a d) grayscale metacarpal image.

generating the binary image of the segmented metacarpal region (Figure 3.7a) was implemented. First, a range operator was applied. The range operator is an adaptive thresholding method in which each pixel is assigned the value of the difference between the $k \times k$ neighborhood maximum and minimum values ($k = 3$ here) (Figure 3.7b). The second step was the application of a simple global threshold based on the mean of the range image to obtain the binary image (Figure 3.7c).

After applying the distance transform, the resultant EDM image (Figure 3.7d) exhibited ridges along the long axis of each metacarpal. After defining the set of image rows that contained five distinct peaks (corresponding to each metacarpal), a grayscale line profile was generated across the center row of this subregion (Figure 3.7e). Working left-to-right, it was known that the fourth peak corresponded to the second metacarpal, and an area around this line profile peak was used to segment the second metacarpal from the rest of the image (Figure 3.7f). To obtain the third, fourth and fifth metacarpal ROIs (Figures 3.8a-c, respectively), the bounding box around the second metacarpal was shifted to the left by 30%, 60% and 70%, respectively, of the total width of the second metacarpal ROI.

When defining the ROI around each metacarpal, the metacarpal located to the left of the metacarpal of interest was included because this improved the success of the subsequent metacarpal segmentation step.

Additional image cropping to eliminate any remaining carpal region was accomplished by excluding image rows proximal to the intersection of the metacarpal and carpal/wrist ridges, which was represented by the highest grayscale value in the EDM image.



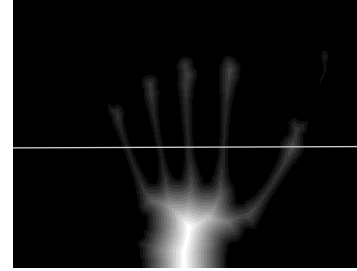
(a)



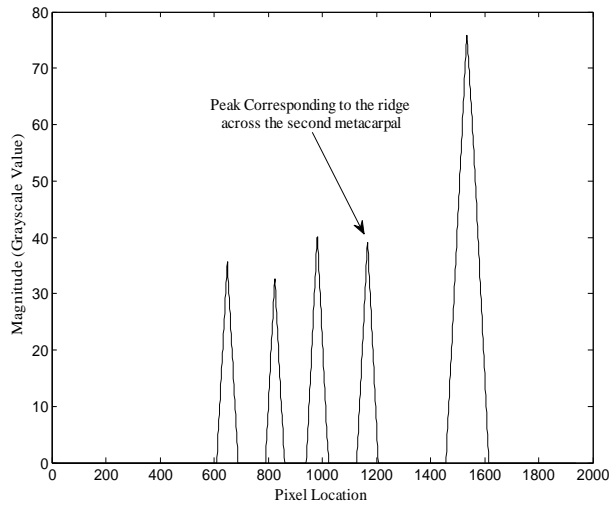
(b)



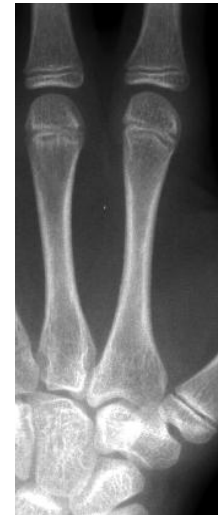
(c)



(d)



(e)



(f)

Figure 3.7. To find the second metacarpal ROI, first a range operator was applied to the a) input grayscale image to obtain b) a contrast-enhanced image. Subsequent thresholding of the contrast-enhanced image yielded c) a binary image of the localized metacarpal region. d) By generating a Euclidean Distance Map (EDM) of the binary image and selecting the brightest portions of the map, we obtained the ridges that correspond to each metacarpal. e) A line profile, was generated at the center location of the region in the EDM where five distinct peaks were present throughout. The peaks in the line profile correspond to the location of each metacarpal. The fourth line profile peak corresponds to the location of the second metacarpal and was used to crop the original image to generate f) a grayscale image of localized second metacarpal ROI.

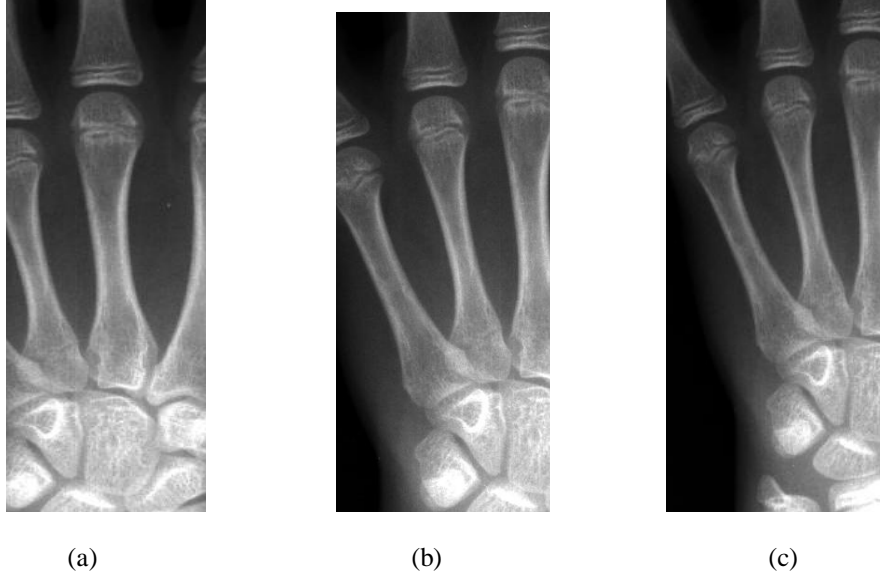


Figure 3.8. To obtain the ROIs for a) the third, b) fourth and c) fifth metacarpal, the bounding box around the second metacarpal was shifted to the left by 30%, 40% and 70%, respectively, of the total width of the second metacarpal. In all cases, the goal was to generate an image that simply contains the entire metacarpal ROI. Additional metacarpal segmentation in the images was handled through subsequent processing steps.

3.3.6 Segmentation of the Metacarpal of Interest

Depending on the age of the subject and on the quality of exposure, simple thresholding to segment the metacarpal of interest was often unsuccessful. Therefore, within each metacarpal ROI, the value corresponding to 0.95CDF of the image histogram was calculated. If this value was below 10,000 (approximately 15% of the total dynamic range) the local image was deemed to be overexposed, and local pre-processing was applied prior to segmentation. The binary image was obtained by logically ‘ANDing’ the result of three, independently processed, precursor images as described in the next sections.

3.3.6.1 Adaptive Thresholding Based on a Range Operator

As described in Section 3.4.4, a range operator was applied, followed by global thresholding (Figure 3.9a). In overexposed images, the global threshold value was reduced by 20% below that used for the rest of the images. Morphological operations, such as closing, were then used to connect disjointed features. After these operations, some pixels inside the metacarpal were still OFF (since the range operator yields very low values inside the metacarpal); these holes were filled using additional logical operations.

3.3.6.2 Adaptive Thresholding based on Local Statistics

In this method, background subtraction was used to enhance areas containing both background and foreground regions. The thresholded image was convolved with a mean operator and subtracted from the original image. The result is expected to be small for homogenous regions and larger for regions with both foreground and background pixels. By thresholding the difference image (again, the threshold was lowered for low contrast images), the area between two different regions was selected (Figure 3.9b).

3.3.6.3 Global Thresholding

The image was thresholded based on a simple global threshold value established by Otsu's method (Figure 3.9c). Since a high global threshold value would likely turn OFF some pixel values inside the metacarpal, the binary image in this step was produced by applying a threshold value that was 50% below the initial threshold value (which is lowered further for low-contrast images). The purpose of this second binary image was to

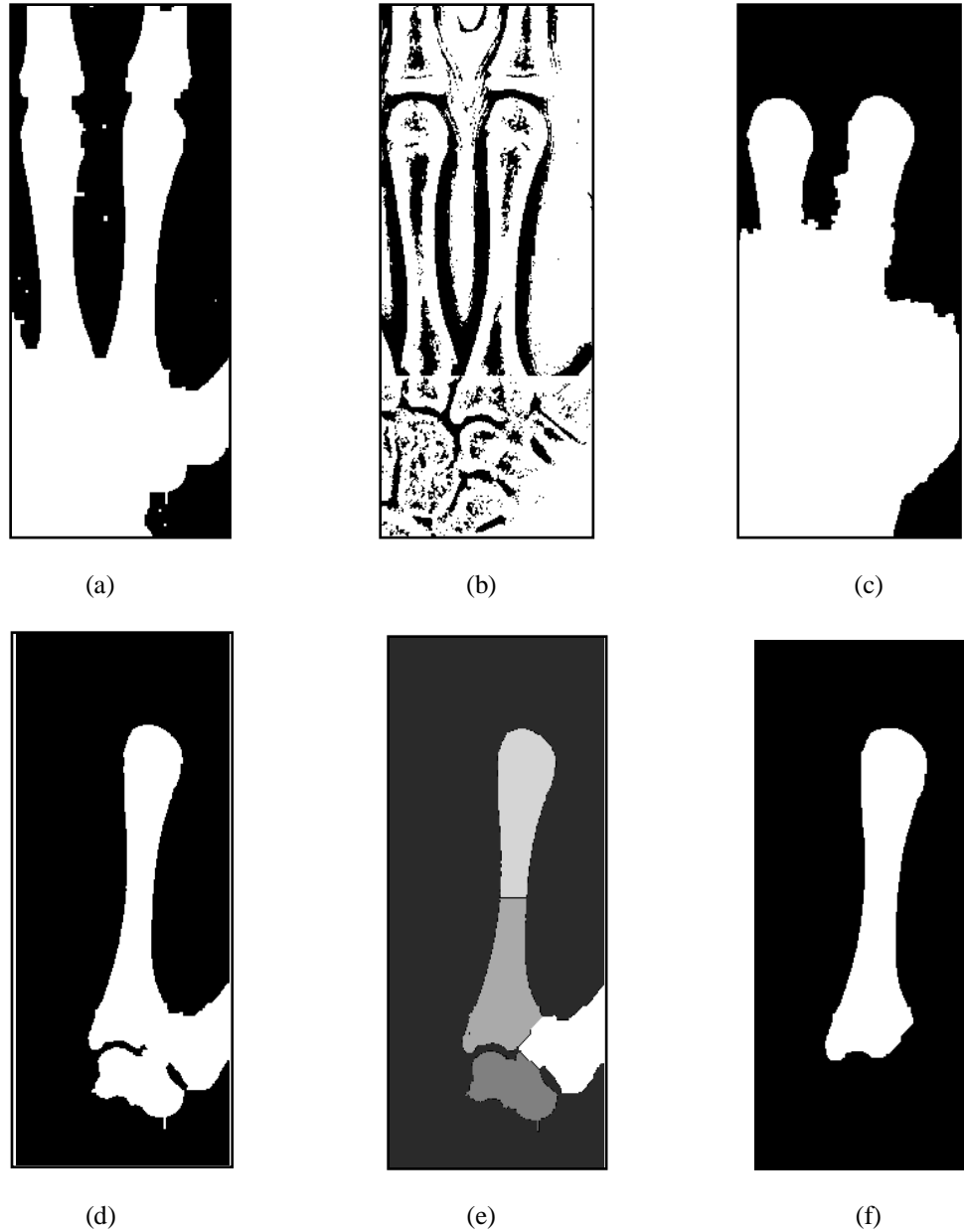


Figure 3.9. To segment the metacarpal of interest, the metacarpal ROI was thresholded using three methods. First a) a binary metacarpal image was obtained through adaptive thresholding by applying a range operator to the image in Figure 3.7f, followed by global thresholding. b) The second binary image was obtained by thresholding the image in Figure 3.7f using adaptive thresholding based on local statistics. Finally, c) the third binary image was obtained by thresholding the image in Figure 3.7f based on Otsu's method. 'AND' logic was then applied to these three binary images and d) the resultant binary image was input to the watershed segmentation process. e) The watershed segmented image gives the boundary between individual objects. f) The metacarpal of interest was selected as the first object reached by moving inward and down from the image's upper right hand corner. If the metacarpal was split into two parts due to low density within the metacarpal (as in (e) here), then both objects representing the metacarpal were selected.

counteract the turning ON of soft tissue regions in the adaptive thresholding methods (Section 3.3.5.1 and 3.3.5.2).

3.3.6.4 Watershed Segmentation

After ‘ANDing’ the results of these three approaches (Figure 3.9d), the watershed method was applied to find boundaries between individual objects. The EDM image shows two overlapping regions with peaks when two structures are touching in a binary image. Each structure can be visualized as a mountain in the EDM image; the mountaintop corresponds to the ultimate eroded points (UEPs) and the intersection of the mountain peaks corresponds to the midpoint between, or intersection of, the structures. To segment the two objects, minima in the valleys between the mountains (called ‘watershed lines’ in reference to how water running down from the mountains would be collected)²³ are connected. The relative height of each mountain is also taken into account during watershed line placement. Structures can then be divided into separate regions by segmenting the image along these contours. Matlab’s ‘watershed’ function was applied to segment each metacarpal (Figure 3.9e). We found that the inclusion of an entire adjacent metacarpal (see Section 3.3.4) resulted in better watershed success when differentiating the metacarpals. If, instead, the metacarpal of interest was initially closely cropped, a portion of an adjacent metacarpal was still likely to be present. In these cases, the small structure would often be considered part of the metacarpal of interest and would not be eliminated by the watershed method.

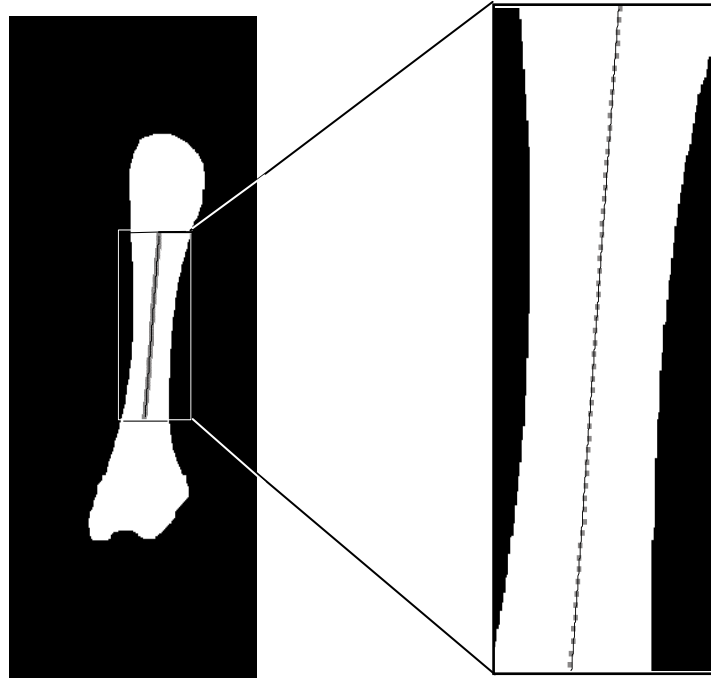
At this point the image for localizing the second metacarpal contained the second and third metacarpals (or a portion of the third metacarpal), the image for localizing the third metacarpal contained the third and fourth (or portion of the fourth) metacarpal, etc. The

metacarpal of interest (Figure 3.9f) was selected as the first object reached by moving inward and down from the image's upper right hand corner. For the fifth metacarpal only (since no sixth metacarpal exists), the metacarpal of interest was selected by moving inward and down from the image's upper left hand corner. In some cases, low density within the metacarpal structure resulted in the watershed method horizontally dividing the metacarpal into two separate structures. In these cases, both objects were selected by walking along the general direction of the long axis of the first object and selecting the second object if it lay along this axis. These objects had only a single row of separation between them, since they were initially connected in the binary image that was input to the watershed method. When the metacarpal was not split, it was possible to avoid picking up the carpals during this process, since there were a number of OFF pixels present between the metacarpals and the carpals in the binary image, which were maintained in the watershed image.

3.4 Measurement and Calculations of Various Parameters of the Metacarpals

3.4.1 Calculation of Total and Diaphyseal Metacarpal Lengths

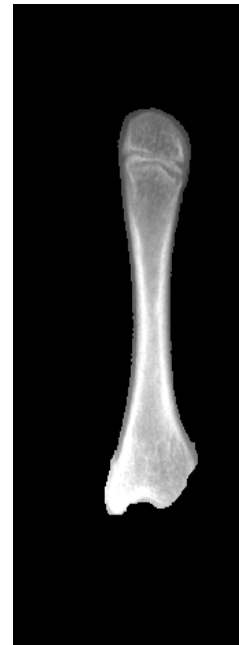
To most easily calculate the total and diaphyseal metacarpal lengths, the segmented metacarpal of interest was first aligned with the vertical axis. Since the shape of the metacarpals is not symmetric, only the middle half of the metacarpal was considered in finding its orientation. The midpoint of the ON pixels in each row was found and a straight line was fitted to these values (Figure 3.10a). The orientation of this line with respect to the vertical axis was calculated by finding the inverse tangent of the line's slope. Using Matlab's 'imrotate' command, which calculates the rotated image using



(a)



(b)



(c)

Figure 3.10. To find the orientation of the metacarpal, a) a line was fit to the midpoints of the ON pixels in each row. b) The mask and the grayscale metacarpal ROI image were then rotated by the negative of the angle found by taking the inverse tangent of the line's slope, and the resulting mask was used to extract c) the grayscale, segmented metacarpal image.

bilinear interpolation, the binary image was then rotated by the negative of the calculated angle (Figure 3.10b) and the center line coordinates were updated. Masking of the original (rotated) grayscale image with the binary image after dilating it by a few pixels, to avoid losing pixels within the metacarpal due to thresholding, yields a vertically-oriented and segmented metacarpal image (Figure 3.10c).

The total and diaphyseal lengths (*TL* and *DL*, respectively) were calculated along the long axis of the metacarpal. The total length extends from the proximal end of the metacarpophalangeal joint to the distal end of the carpal-metacarpal joint. These points correspond to the locations of maximum gradients on the line profile taken along the central axis of the metacarpal (Figure 3.11). After calculating the first difference array along the line profile, the maximum positive difference value corresponded to the distal metacarpal edge, whereas the maximum negative value corresponded to the proximal edge (Figure 3.12). If the diaphyseal/epiphyseal fusion was not yet complete, the metacarpal diaphyseal length was also calculated. A local maximum gradient between the two metacarpal endpoints corresponds to the point at which diaphyseal/epiphyseal fusion is initiated (Figure 3.13). To determine if a diaphyseal length should be calculated, we checked the following two conditions for each peak location in the line profile: (1) Does the peak lie within a distance of 120 pixels (approximately 11 mm) from the distal edge location? And (2) does the peak have a magnitude greater than 65% of the negative peak value at the proximal edge location? If both conditions were met, the diaphyseal length was calculated.

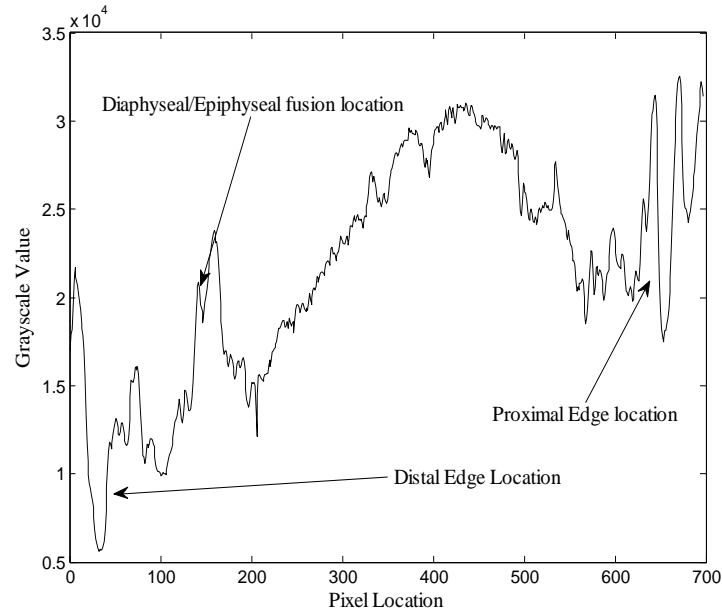
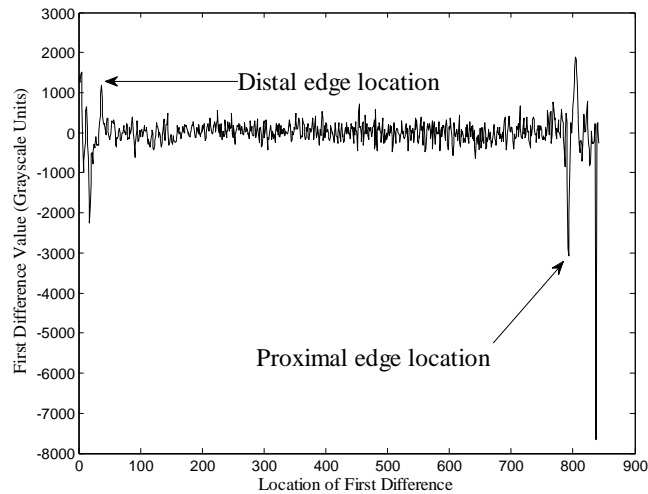


Figure 3.11. The line profile taken along the long axis of the metacarpal shows the grayscale variation along the total length of the metacarpal, extending from the distal edge location to the proximal edge of the metacarpal. If a diaphyseal length should be determined, it is calculated as the length of the line extending from the location of the diaphyseal/epiphyseal fusion location to the distal edge location of the metacarpal.

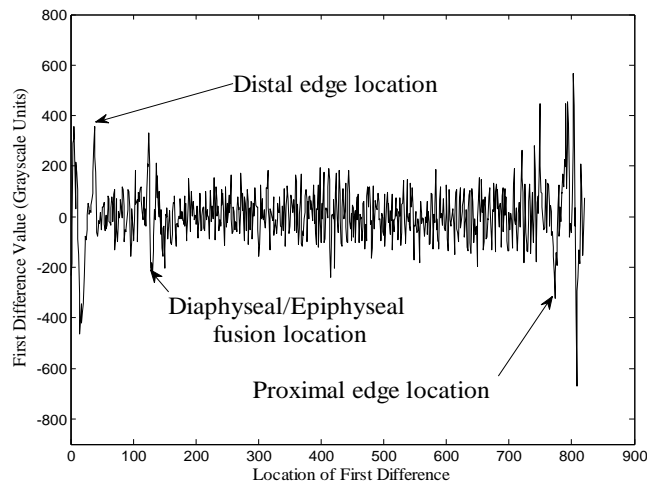


(a)



(b)

Figure 3.12. To find the total length of the metacarpal, a) a plot of the first difference of the line profile was generated along the long axis of the metacarpal. The location of the maximum gradients at the two ends of the curve (after coming in a few pixels from the both the ends) correspond to the distal and proximal edge locations of the metacarpal. b) The distance between these two end points is equal to the total length of the metacarpal.



(a)



(b)

Figure 3.13. To find if there exists a diaphyseal length, the first difference of the line profile across the long axis of the metacarpal was computed. a) If, between the ends of the metacarpal, a peak exists that satisfies both of the following two conditions: (1) it lies within a distance of 120 pixels from the distal edge location and (2) it has a magnitude greater than 65% of the negative peak value at the proximal edge location, then a diaphyseal length should be computed. Here a peak was selected as the diaphyseal/epiphyseal fusion point and b) the diaphyseal length was then calculated as the distance between the diaphyseal/epiphyseal fusion point and the proximal edge of the metacarpal.

3.4.2 Calculation of the Total Midshaft, Diaphyseal Midshaft and Minimum Shaft

Width Locations

Cortical widths were assessed at three locations in the metacarpal: at the total midshaft position, at the diaphyseal midshaft position and at the position of minimum shaft width. The diaphyseal and total lengths were used to calculate the diaphyseal midshaft and total midshaft position, respectively. In each case, the midshaft position lies exactly halfway between the segment ends. To find the position of minimum shaft width, the metacarpal diameter was calculated at each row along the middle 50% of the metacarpal, and the position of the minimum diameter was stored.

3.4.3 Location of the Endosteal and Periosteal Edges

Radiographs record the projection of three dimensional structures onto a two dimensional space. Consider a transverse cross-section of a simplified metacarpal, constructed using simple geometry and homogenous material densities (Figure 3.14). If we sum, column-wise, the grayscale values in that representation, the result represents the total material path length and density seen by the x-ray beam at that location. The array of column-wise sums represents the projection recorded in the PA hand radiographs at each row position. The highest grayscale value in that line profile (row) corresponds to the position at which the x-ray beam passes through the maximum amount of material/density. In our case, that occurred when the beam passed through the maximum amount of cortical bone. Assuming a cylindrical metacarpal cortex, and both symmetric and homogenous soft tissue and marrow cavity distributions, this position of highest grayscale value occurred at the endosteal edge.

Referring again to Figure 3.14, the periosteal edge can be found at the position between the outer soft tissue region and the endosteal edge, at which the line profile exhibits maximum curvature. For image analysis, this location was found by taking the first difference of the line profile, finding all candidate peaks with magnitudes between 70% of the medial (positive) peak and 70% of the lateral (negative) peak and selecting the outermost peaks, which corresponded to the medial (transition from soft tissue to bone) and lateral (transition from bone to soft tissue) periosteal edges, respectively (Figure 3.15a).

3.4.4 Calculation of Medial and Lateral Cortical Thicknesses and Derived Parameters

The medial/lateral cortical thickness (Figure 3.15b) is the difference between the medial/lateral periosteal and endosteal edge positions; the number of pixels between these locations was calculated and the result was multiplied by the known pixel dimension (85 μm). Additional measurements derived from the edge locations included the total bone diameter (difference between the medial and lateral periosteal edge positions) and the medullary diameter (difference between the medial and lateral endosteal edge positions). The total cortex, cortical index, polar moment of inertia and polar section modulus were then calculated using Equations 2-5.

Multiple corrections were made to found edge locations. Some are due to known shifts in the edge and others are made to allow the user to easily arrive at consistent decisions when manual adjustments to the edge locations are required. The two known edge shift issues are the half-pixel shift when using gradient information (difference arrays) and the blur correction.

3.4.5 Calculation of Blurring Correction Factor

Among others, two known factors contributed to measurement accuracy. Here we present the correction process for both known errors. The first issue was edge blurring due to the finite dimensions of the x-ray tube focal spot. Although the actual x-ray tube used during image acquisition has changed over the course of the FLS study, we were limited to experimentally determining that parameter for the current set-up only. To develop the blur correction, the image of an aluminum step wedge was acquired from the current

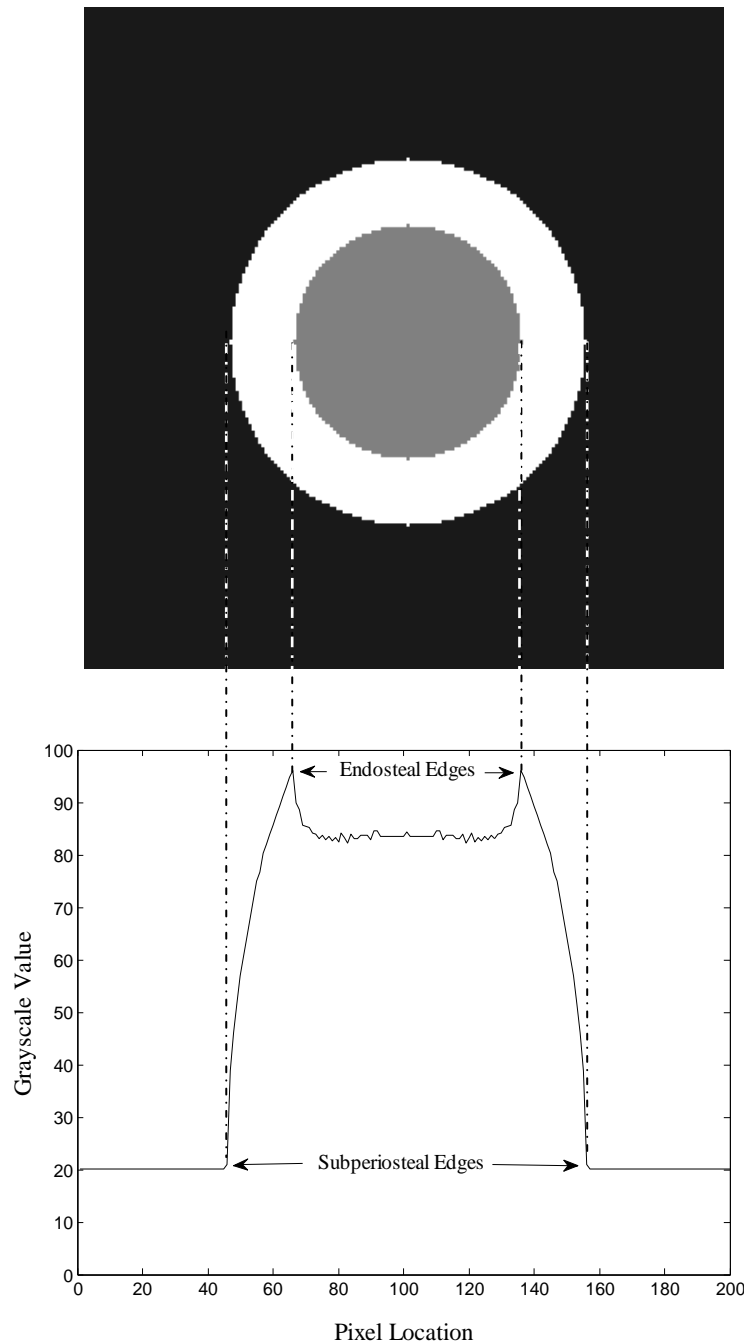
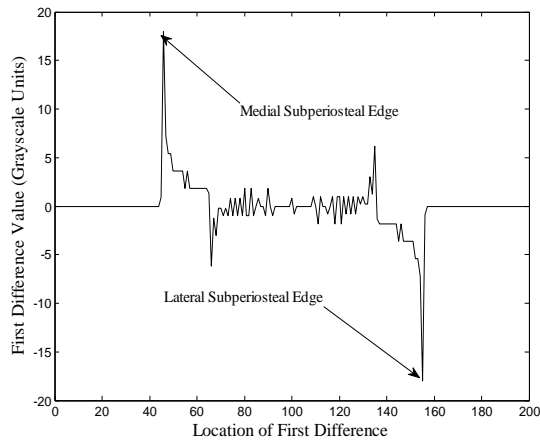
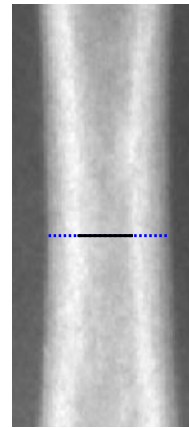


Figure 3.14. To review the edge locations from the metacarpal projection image, a transverse cross-section of the metacarpal was simulated using two concentric circles with homogenous density values. A “density” value of 0.5 was associated with the inner circle to simulate medullary cavity. The region between the inner and outer circle was given a value of 1 to simulate the cortical bone. Finally, a “density” value of 0.1 was given to the region outside both circles to simulate soft tissue. The highest grayscale value in the projection occurs when the x-ray beam passes through the maximum amount of material/density, which in the case of the metacarpal corresponds to the endosteal edges. The periosteal edges lie between the soft tissue and the cortical bone and are represented as the points of maximum curvature (gradient) in the soft tissue-bone transition region.



(a)



(b)

Figure 3.15. To find the maximum curvature points along the metacarpal line profile corresponding to the periosteal edges across the metacarpal, the maximum gradient was found in a) the first difference of the line profile (data for this plot were generated from simulation described in Figure 3.14). Based on the periosteal and endosteal edge locations, the dimensions of b) the medullary cavity (solid line), the medial and lateral cortical thickness (dashed lines), and the total diameter (dashed plus solid lines) were calculated.

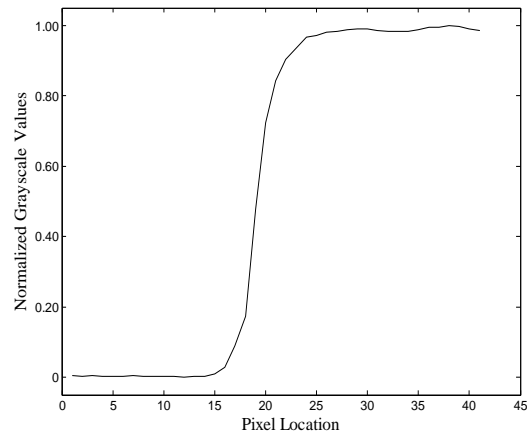
x-ray system (Figure 3.16a), and a line profile across the wedge was extracted (Figure 3.16b). This line profile was then compared to the profiles found by convolving a perfect edge profile (Figure 3.17a) with different blurring functions (Gaussian kernels with different values of sigma (Figure 3.17b)). The blur factor (sigma) that yielded the highest correlation coefficient between the experimentally measured line profile and the ideal edge under that blur indicated the best approximation of the actual system blur (Figure 3.17c).

Because the ideal edge profile exists only for step objects of constant material density and thickness (such as a slab), and because we recognized that our object does not fall into that class of objects, we wanted to separately assess the effect of object shape on measured edges. To simulate the expected line profile across the metacarpal, we first

generated a test image consisting of two concentric circles that represented cortical bone. The region outside the outer circle was assigned a low grayscale value to simulate soft



(a)



(b)

Figure 3.16. To find the blurring function of the system, a) an image of a step wedge was acquired with the x-ray tube currently used in the FLS and b) a line profile was generated at a location across the edge of the step wedge perpendicular to the long edges of the wedge (solid line in (a)).

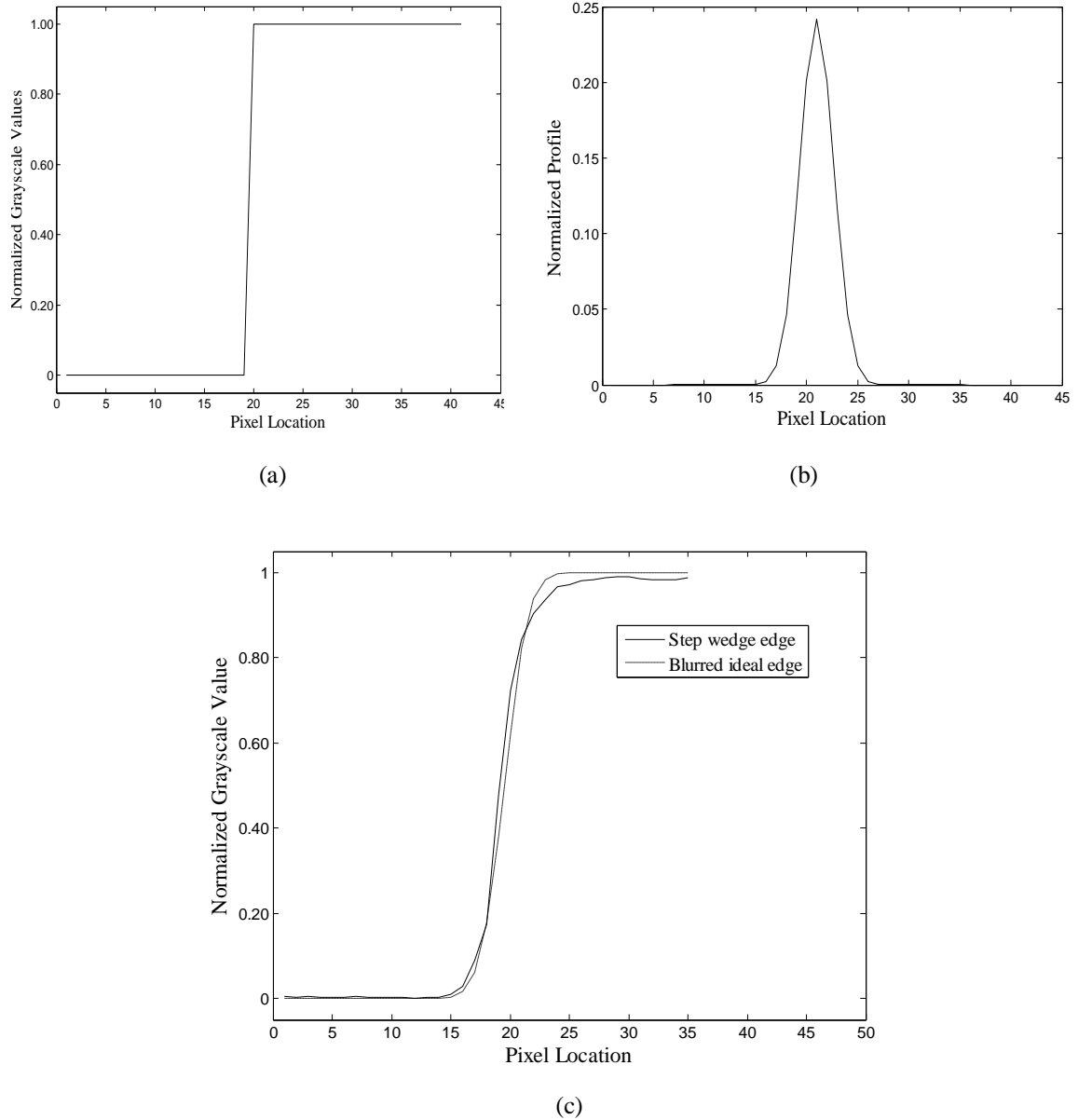


Figure 3.17. Assuming that the imaging system's point spread function can be modeled as a Gaussian blur, a) the line profile of an ideal edge was blurred with different blurring functions (Gaussian kernels with different values of sigma) to find the sigma of the blurring function. b) The blurring factor (sigma), which yielded the c) highest correlation between the simulated blur edge and the experimentally determined blur edge gives the best approximation of the actual system blur.

tissue, the region between the two concentric circles was assigned a high grayscale value to simulate cortical bone, and the innermost region was assigned an intermediate grayscale value to simulate trabecular bone and bone marrow.

The values across each image column were summed to achieve the ideal (non-blurred) line profile, and this profile was then blurred with the experimentally-determined blur function. The amount of periosteal edge shift and endosteal edge shift in the blurred line profile were found by comparing the original and the blurred line profiles.

3.4.6 Half Pixel Shift in the Edge Locations

The second known issue was due to the pixelation of our image data. As we used first differences to locate the positions of maximum gradients in the line profiles, we needed to store the calculated difference values in a corresponding array. The actual edge lies between the two pixels that yielded the maximum difference, yet we must store the difference value at one of the two locations. The first pixel of the edge pair was selected for storing the edge information, so the required half-pixel shift is +0.5. Although the storage scheme is consistent across the profile, we felt that the analyst should not have to understand this aspect of the program. Our solution was to store the periosteal edge information at the position of the roof (the highest grayscale value along an edge transition) for both the medial and lateral edges (Figure 3.18) and make the adjustment within the program so that the user always moves the periosteal markers to the “top” of the maximum gradient on the profile. The appropriate half-pixel shift is then -0.5 for the medial periosteal edge and +0.5 for the lateral periosteal edge (Figure 3.18) toward the floor (the lowest grayscale value along an edge transition). The half-pixel shift issue is slightly different for the endosteal edges, which are found from peaks in the line profile. Referring to Figure 3.14, the actual endosteal edge lies between the position at which the maximum amount of bone is present and the neighboring pixel that represents bone and

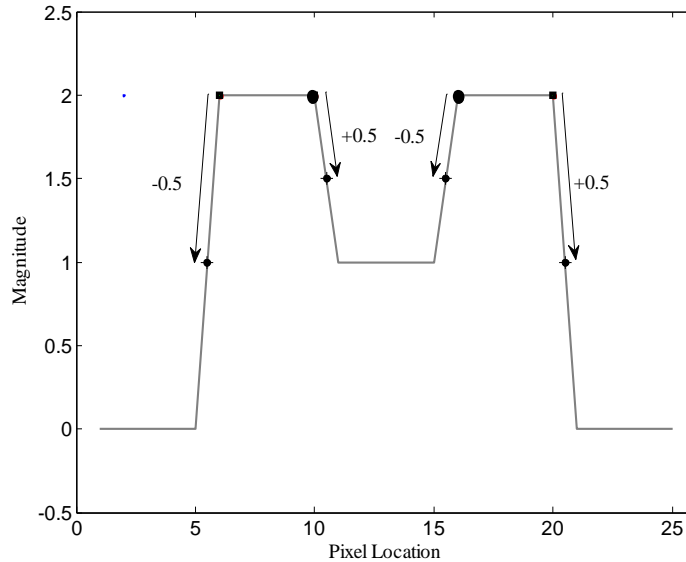


Figure 3.18. The half-pixel shift is illustrated here for the endosteal and the periosteal edges. The square markers indicate periosteal edge locations (pixel locations 6 and 20) and the circular marker indicate endosteal edge locations (pixel locations 10 and 16) after the storage scheme has been adjusted for storing the edge locations at the roof of the edge. The shift in the periosteal edges is away from the center because again the roof was selected for storing the periosteal edge locations and the thickness between the two edges was underestimated by one pixel. The shift in the endosteal edge location is toward the medullary cavity (the floor of the edge transition), because the endosteal edge locations were stored at the roof, leading to an overestimation of the cortical thickness by one pixel..

marrow material. In marking the endosteal edge, the user positions the marker at the position of the peak and the half-pixel adjustment is a 0.5 shift toward the medullary cavity.

3.5 Phantom Study to Assess Method Accuracy

To validate the approach for finding periosteal and endosteal edges, a phantom with known dimensions (Figure 3.19) was imaged using the current FLS x-ray system. The phantom dimensions were verified by manual measurements and were found to agree within 0.1 mm to the literature value. Magnification corrections were applied using

Equation 1, and the actual phantom dimensions were compared to those obtained through the automatic analysis.

Since the centers of each cylinder step within the outer Plexiglas cylinder lie along the same line, the object-to-film distance was taken from the cylinder's center axis to the center of the cassette, in which the film is placed, yielding a source-to-object distance D_{so} of 982 mm. The source-to-film distance D_{sf} was 1016 mm (40 inches). The calculated magnification factor M of 1.0346 was applied to the actual phantom dimensions before comparison to the dimensions calculated using the software. As with metacarpal analysis, the long axis of the phantom image was rotated so as to align it with the vertical image axis (Figure 3.20). The dimensions of each cylinder step were calculated at ten individual rows (object cross-sections) within the step, the half pixel shift and blurring corrections were applied to each result and the measurements were averaged to obtain the dimensions of each cylinder step. Results of the phantom study are summarized in Table 3.2.

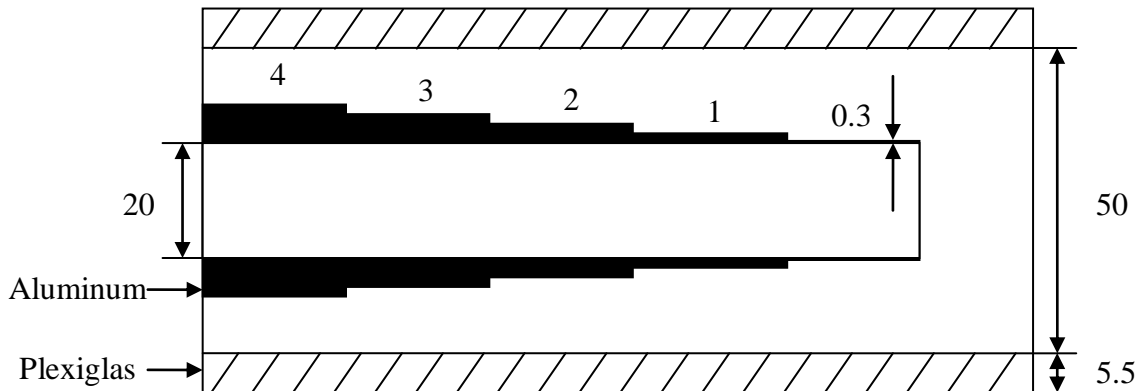


Figure 3.19. Cross-section of the aluminum cylindrical step phantom used to validate the edge finding methods. The aluminum thickness within the cylindrical step phantom decreases with the outer diameter of the step. The aluminum pieces is enclosed within a Plexiglas cylinder. All dimensions are in mm. Figure based on 24.

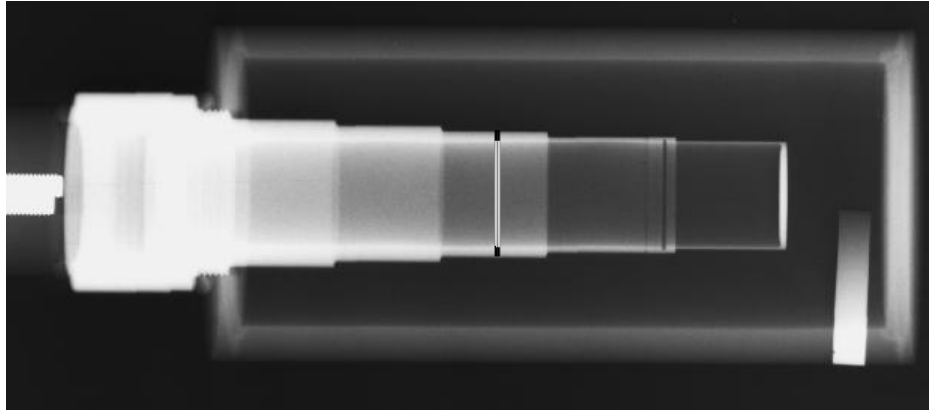


Figure 3.20. Radiograph of the cylindrical step phantom imaged using the current x-ray system at FLS. The acquired image was used to assess the accuracy of our software in finding outer and inner edges of cylindrical objects. The white and the black lines indicate the positions at which outer cylinder widths and wall thicknesses were measured. These measurements were compared to the known dimensions of the phantom at that location.

The agreement between the actual and measured phantom dimensions was very high, exceeding 99% at every step. We concluded that the edge finding method applied was quite accurate for the measurement of a cylindrical object.

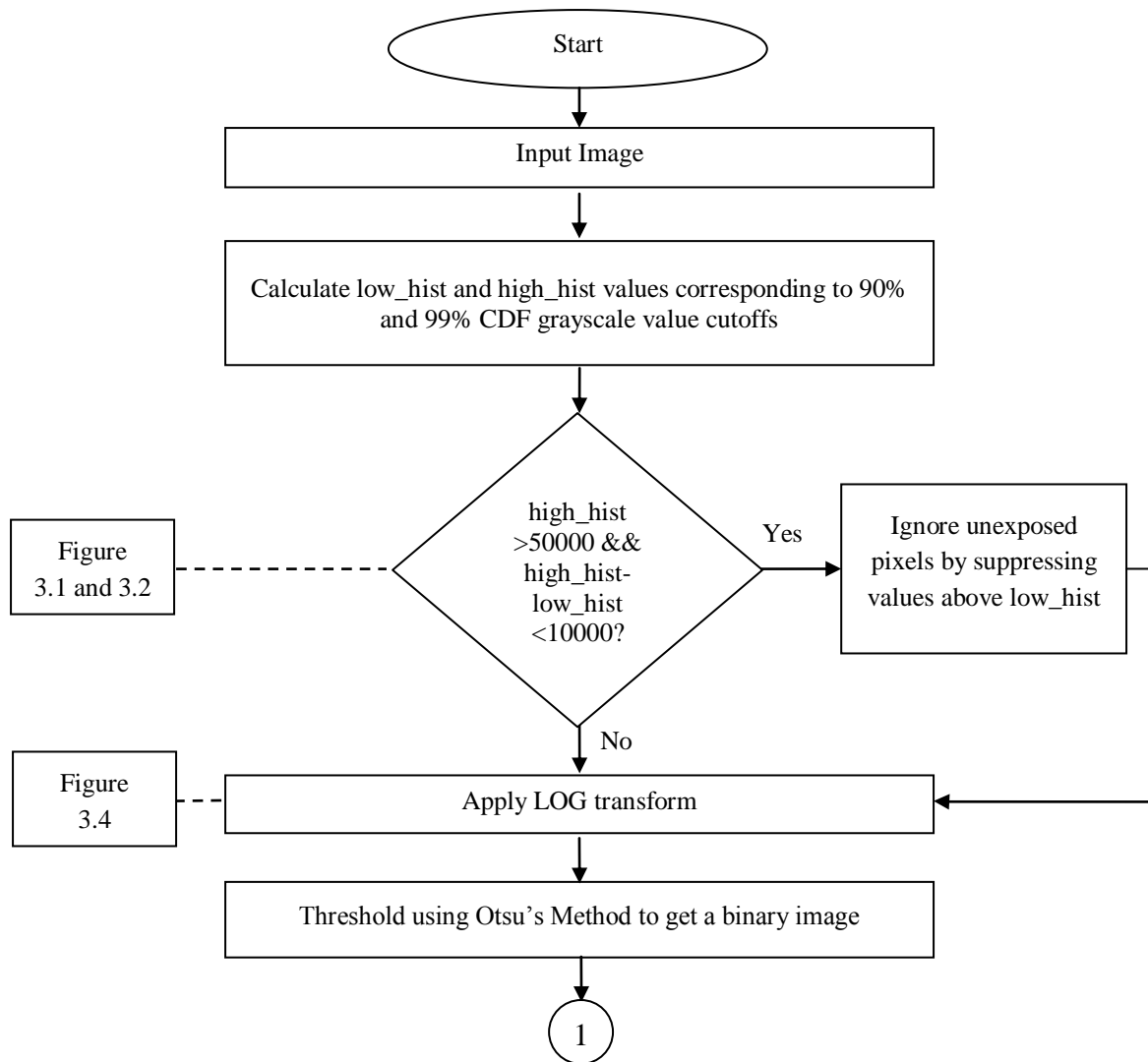
To validate the automated method for calculating total cortical thickness, the total thickness of aluminum wall at the 24 mm step (4.12 mm, since the inner hollow cylinder diameter found was 19.82 mm) was calculated using the automated software. This position on the phantom was selected because the total aluminum wall thickness most closely approximates the normal adult metacarpal cortical thickness (Figures 3.19 and 3.20). The automatically calculated total wall thickness of 4.0640 mm was compared to the magnified true total wall thickness of 4.2625 mm, representing an accuracy of 4.65%. The accuracy error while finding the total cortical thickness that consists of overall four edges, is 0.1985 mm which is less than three pixels, hence giving subpixel accuracy while finding each edge location.

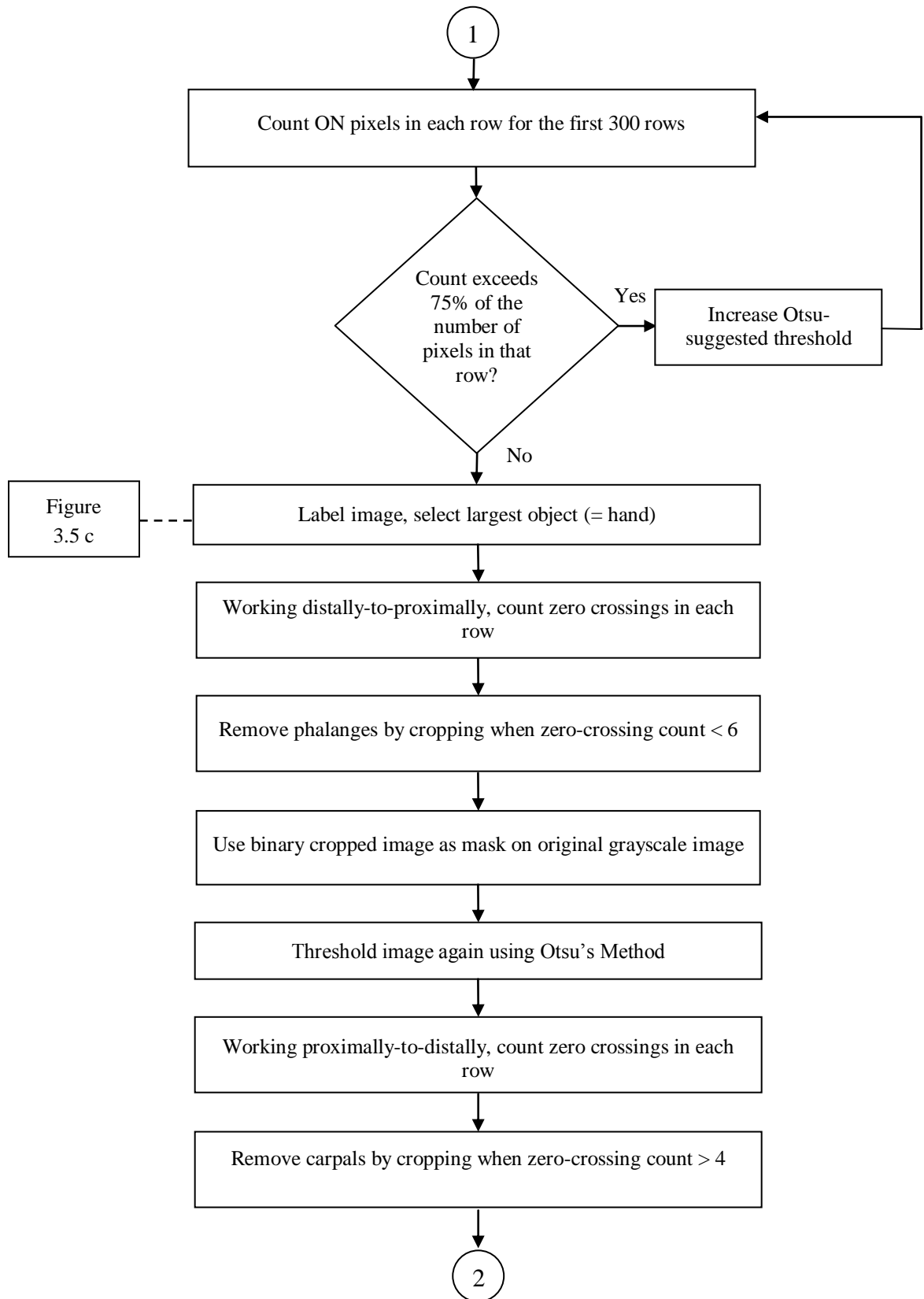
Table 3.3: Phantom results to assess the accuracy of the automated analysis routines.

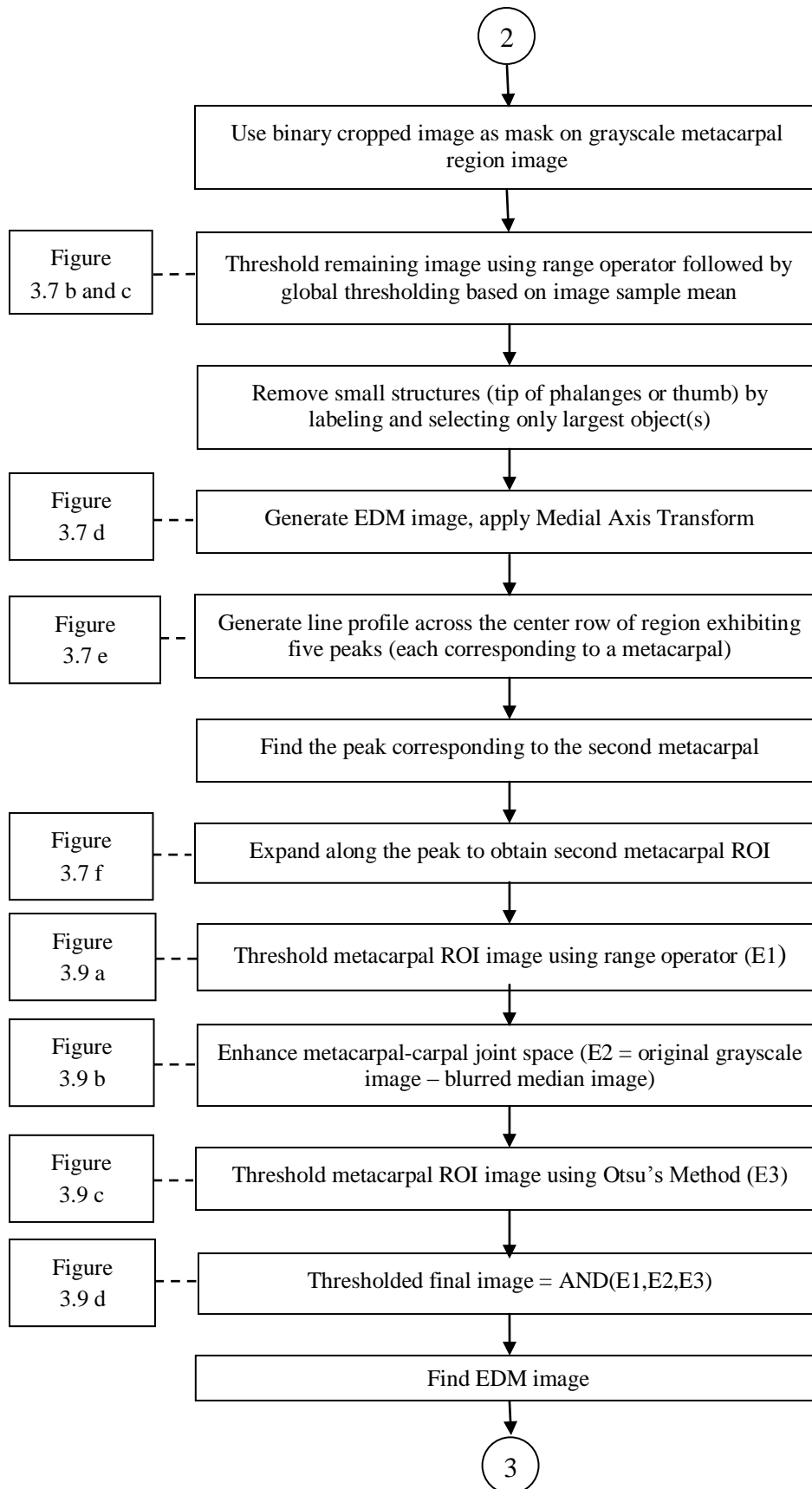
Periosteal Edge					
Step	Actual Cylinder Outer Dimension [mm]	Expected Cylinder Image Dimension (Magnification Correction Applied) [mm]	Cylinder Dimension Obtained with Automated Analysis (Includes Half-Pixel Shift and Blur Corrections) [mm]	Difference Between Actual and Measured Dimensions [mm]	Accuracy Error [%]
1	20.6	21.31	21.34	0.03	0.14%
2	22	22.76	22.69	0.07	0.31%
3	24	24.83	24.74	0.09	0.36%
4	26	26.89	26.70	0.19	0.71%
5	28	28.96	28.73	0.23	0.79%
Cortical Thickness					
3	4.12	4.2625	4.0640	0.1985	4.65%

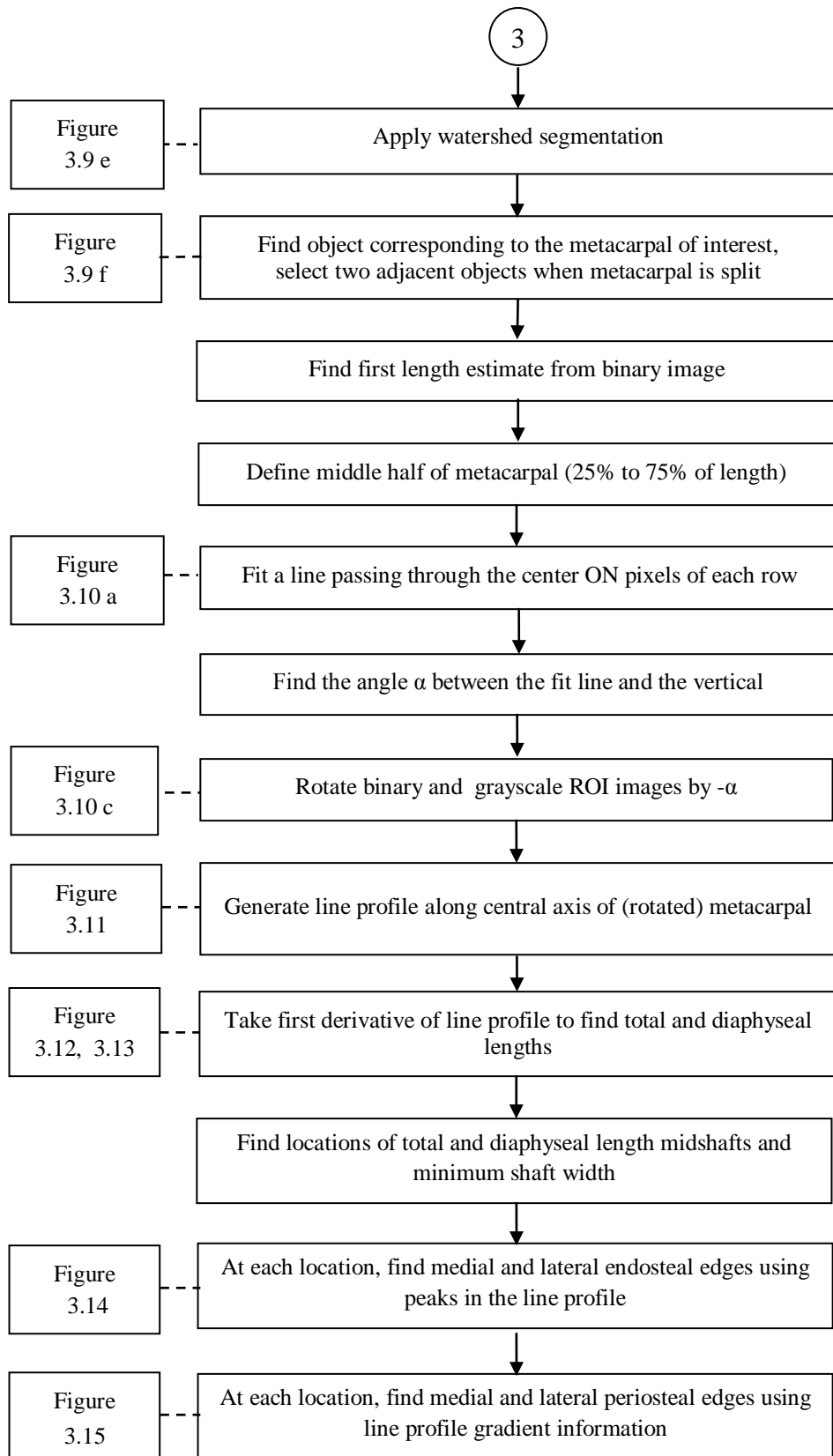
3.5 Flowchart

A flowchart of the automated analysis procedure is provided here. The steps below detail how the second metacarpal analysis is performed. The third, fourth and fifth metacarpal analyses are carried out using this same approach.









4. GRAPHICAL USER INTERFACE

A graphical user interface (GUI) provides the software user with a pictorial view of the algorithm to assist with program interaction. Using Matlab's Graphical User Interface Development Environment (GUIDE) (Matlab R2007b, MathWorks, Inc., Natick, MA, USA) we developed an interface with various user interaction tools, such as display panels, pushbuttons, radio buttons, text boxes, etc.

4.1 Requirements of the GUI

The GUI serves to provide the output (images, line profiles and calculated data) of the automated analysis process and to offer tools for the user to correct the process at various stages in the event that the output of the automatic routines is incorrect. User intervention is possible at the following stages: metacarpal selection, metacarpal segmentation, diaphyseal and total length calculation and cortical thickness calculation.

4.2 Components of the GUI

The main GUI was designed to meet the stated requirements of automatic analysis and manual intervention (Figure 4.1). During the GUI design phase, feedback from the client was incorporated to generate a user-friendly tool to accomplish the analysis. Details of each GUI section are described below.

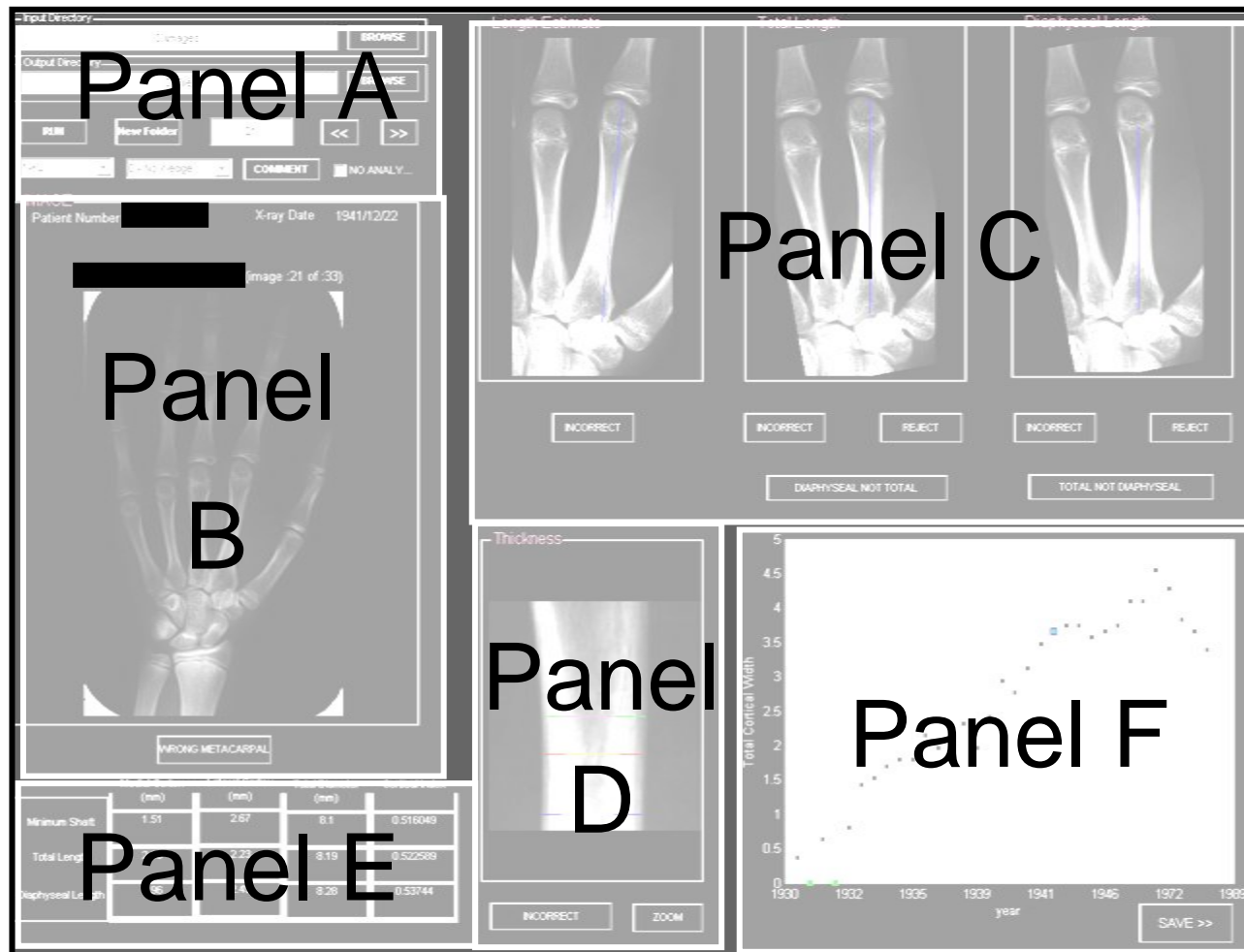


Figure 4.1. Layout of the main GUI. Each panel guides specific tasks as explained in detail in subsequent figures.

4.2.1 Selection of the Input and Output Directory, Assessor and Wedge Type

To initiate the analysis procedure, the user first copies the images to be analyzed to a particular directory. The GUI is then invoked in Matlab, and within Panel A (Figure 4.1), using the 'BROWSE' button (Figure 4.2, Item 1), the analyst selects the input directory that contains the participant folders, and then clicks the 'RUN' button (Figure 4.2, Item 2). This causes the program to be executed sequentially for all images in all participant folders in the input directory. It is envisioned that this operation will run overnight and that the results will be reviewed by the analyst on the following day. During program execution, individual output .mat files containing the full analysis results (subimages, point locations, calculated parameters, etc.) are generated for each image inside the individual folders created for each of the participants and stored at the location 'C:\mat_files_final' (Table 4.1). When the analyst is ready to review the automated analysis results, clicking the 'BROWSE' button (Figure 4.2, Item 3) associated with the output directory prompts for the path name of the location in which the output file will be stored. The user also inputs the assessor information (the analyst's initials) along with the calibration wedge type present in the image (the default is '0-No Wedge') (Figure 4.2, Items 4 and 5). Clicking on 'New Folder' (Figure 4.2, Item 6) retrieves the first image in the first folder within the directory of analyzed images and displays the original full image in GUI Panel B. At any time, the user can advance to the next or previous image within a folder by selecting the '>>' or the '<<' buttons in Panel A (Figure 4.2, Item 7). The user can also go to a specific image in the folder by inputting the image number in the text box next to the 'New Folder' button (Figure 4.2 Item 8), and then selecting the

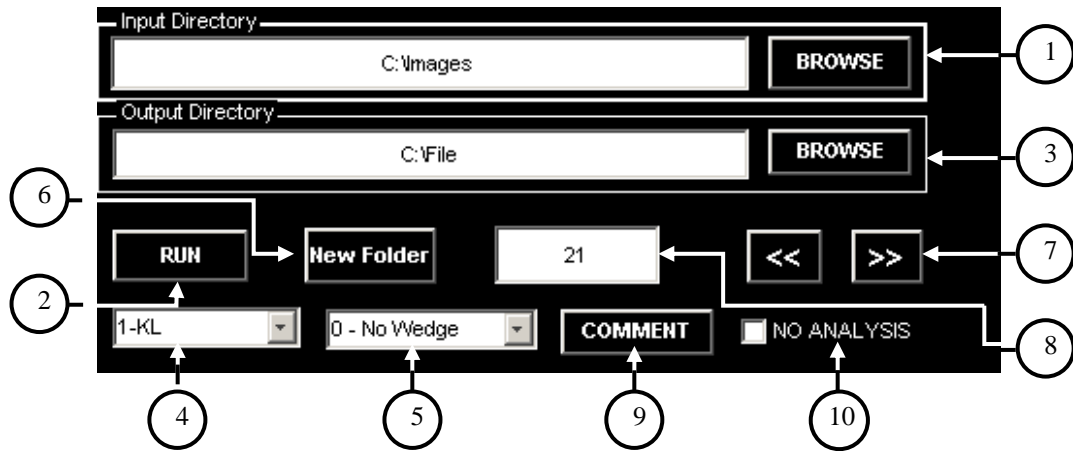


Figure 4.2: Layout of Panel A. The user initiates the analysis by selecting the input directory using the (1) Input Directory ‘BROWSE’ button and then selecting (2) ‘RUN’. To view the automated analysis results, first the output directory is selected using the (3) Output Directory ‘BROWSE’ button, and then the (4) assessor information and (5) wedge type are input. Selecting the (6) ‘New Folder’ button then displays the first image in the first folder (and increments the folder number when it is subsequently selected). To go to the next or previous image, the user selects (7) the ‘>>’ or the ‘<<’ button; to jump to a particular image in the folder, the image number may be directly entered in the (8) edit box before selecting the ‘>>’ button. The user can also enter narrative comments as needed using the (9) ‘COMMENT’ button. The (10) ‘NO ANALYSIS’ button is selected to save NaN values in the output file for images that cannot be analyzed (either automatically or manually).

‘>>’ button. If the user wants to include a narrative comment in the output file, selecting the ‘COMMENT’ button (Figure 4.2, Item 9) will open a new window for this purpose. The user can type the comment or make changes to the previously stored comments. Finally, if a particular image cannot be reliably analyzed (due, for example, to very low contrast or a high degree of rotation) then user can check the ‘NO ANALYSIS’ box (Figure 4.2, Item 10) which will cause NaN to be written for all variables in the output file.

4.2.2 Viewing the Output of the Automated Segmentation Process

The results of automated segmentation are displayed on the right hand side of the GUI (Figure 4.1 Panel C). For the metacarpal of interest, the image of the segmented metacarpal and a line along its approximate length are displayed in the ‘Length Estimate’

Table 4.1. Essential auto-analysis results variables are stored in individual .mat files, which are used to quickly re-generate images and results to display in the GUI for review by the analyst.

	Variable Name	Variable Description
1	rect_points	Coordinates of metacarpal ROI in original image
2	image_line1	Coordinates of the approximate length line
3	Angle	Inclination of the metacarpal in original image
4	Ccrop	Column value corresponding to the long axis of the metacarpal
5	L3	Binary image of the segmented metacarpal
6	Lengths	Row location of metacarpal distal and proximal edges, epiphysis/diaphysis location. Dummy values (zeros) are stored if this does not apply.
7	total_pos	Row position (along long axis) of the midshaft of total length
8	diaphyseal_pos	Row position (along long axis) of the midshaft of diaphyseal length
9	min_pos	Row position (along long axis) of the position of minimum shaft width
10	total_cortical_thickness	Periosteal and endosteal edge locations at midshaft of total length
11	diaphyseal_cortical_thickness	Periosteal and endosteal edge locations at midshaft of diaphyseal length
12	minimum_cortical_thickness	Periosteal and endosteal edge locations at minimum shaft width

window. The rotated metacarpal image and lines representing its total and diaphyseal lengths are displayed in the ‘Total Length’ and ‘Diaphyseal Length’ windows, respectively. In the ‘Thickness’ window, a zoomed in version of the metacarpal midshaft region is provided and three different colored horizontal lines that correspond to the

position of the total midshaft, diaphyseal midshaft and minimum shaft width are superimposed on the image. Each line is comprised of three line segments; the outer two segments show the calculated widths of the medial and lateral cortex, and the center line segment shows the width of the medullary canal. (Figure 4.1 Panel D). A table of results (Figure 4.1 Panel E) displays the values of the total bone diameter, along with the medial and lateral metacarpal cortical widths and the cortical index. A plot of total cortical width at the position of minimum shaft width as a function of the radiograph acquisition date is displayed for each participant (Figure 4.1 Panel F), giving the user visual feedback of individual image results as well as the trend of total cortical width with respect to visit date. The point in this plot corresponding to the currently viewed radiograph is highlighted in a different color. To accept and store the results for the current image, the user presses the ‘SAVE >>’ button. Output variables (Table 4.2) are written to the output file (an excel spreadsheet) with each spreadsheet row corresponding to one image in the current folder. Once review of all images in a participant’s folder is complete, the user can select the next folder by selecting the ‘New Folder’ button.

4.2.3 Correction for Wrong Metacarpal

Depending on image quality, patient positioning, patient anatomy, etc., the automated analyses can fail at one or more processing steps. The GUI provides options for user intervention at different stages in the processing. Often, correcting an upstream error will allow the processing to complete successfully. Next to each image output in Panels B, C and D are buttons that invoke user corrective actions for that particular processing step. First, if the incorrect metacarpal region is selected, pressing the ‘INCORRECT’ button

Table 4.2: Variables stored in the output file (an excel sheet) after the user accepts the results by pressing the ‘SAVE >>’ button. Analysis results of one metacarpal of one image are written to the output file with each SAVE button. The output for all metacarpals is stored in single row of the output file. Analysis results for subsequent images of that participant are stored in subsequent rows (one row per image).

Field	Variable Name	Variable Description	Comments
1	IDCODE	Identification code for participant (alpha-numeric)	e.g., FEL00001 or FEL00247
2	PTNO	Participant number (numerical)	e.g., 1 or 247
3	VISIT	Visit date	Eight digit date, e.g., 20080509
4	YEAR	Visit year	Four digit year, e.g., 2008
5	MONTH	Visit month	Two digit month, e.g., 05
6	DAY	Visit day	Two digit day, e.g., 09
7	WEDGE	Type of wedge	Drop-down list of 12 wedge types
8	MULTIX	Multiple radiograph designation	A and B represent first and second radiograph at visit; 1 designates best radiograph if multiple available
9	COMMENT	Comments regarding radiograph	Comment text field
10	MC2MISS	MC2 is missing	Default is 0; 1 indicates missing metacarpal
11	MC2DATE	MC2 date of analysis	Eight digit date
12	ASSESSOR	Initials of the user	User initials are in dropdown menu
13	MC2LINE	MC2 line profile adjusted by user	Default is 0; 1 indicates manual adjustment by user
14	MC2 LPeak	MC2 lateral peak value at the minimum shaft location	Used to calculate quality index
15	MC2MPeak	MC2 medial peak value at the minimum shaft location	Used to calculate quality index
16	MC2LTROUGH	MC2 trough location between the peaks	Used to calculate quality index
17	MC2LQUALP	MC2 bone quality at the lateral side w.r.t. the peak value	$MC2LPeak - MC2TROUGH / MC2Lpeak$
18	MC2MQUALP	MC2 bone quality at the medial side w.r.t. the peak value	$MC2MPeak - MC2TROUGH / MC2Mpeak$
19	MC2LQUALT	MC2 bone quality at the lateral side w.r.t. the trough value	$MC2LPeak - MC2TROUGH / MC2TROUGH$
20	MC2MQUALT	MC2 bone quality at the medial side w.r.t. the trough value	$MC2MPeak - MC2TROUGH / MC2TROUGH$
	Variable Name	Variable Description	Comments

Field			
21	MC2TL	MC2 total length	Two decimal places
22	MC2DL	MC2 diaphyseal length	Two decimal places
23	MC2TMD	MC2 midshaft diameter taken at midshaft of total length	Two decimal places
24	MC2TMC	MC2 medial cortex taken at midshaft of total length	Two decimal places
25	MC2TLC	MC2 lateral cortex taken at midshaft of total length	Two decimal places
26	MC2TMED	MC2 medullary diameter at midshaft of total length	Two decimal places
27	MC2TTC	MC2 total cortex at midshaft of total length	= MC2TMC + MC2TLC
28	MC2TCI	MC2 cortical index at total midshaft	= MC2TTC / MC2TMD
29	MC2TJ	Polar moment of inertia at midshaft of MC2 total length	= $\pi/32 * (MC2TMD - MC2TMED)$
30	MC2TZP	Polar section modulus at midshaft of MC2 total length	= MC2TJ / (MC2TMD / 2)
31	MC2DMD	MC2 midshaft diameter taken at midshaft of diaphyseal length	Two decimal places
32	MC2DMC	MC2 medial cortex taken at midshaft of diaphyseal length	Two decimal places
33	MC2DLC	MC2 lateral cortex taken at midshaft of diaphyseal length	Two decimal places
34	MC2DMED	MC2 medullary diameter taken at midshaft of diaphyseal length	Two decimal places
35	MC2DTC	MC2 total cortex at midshaft of diaphyseal length	= MC2DMC + MC2DLC
36	MC2DCI	MC2 cortical index at diaphyseal midshaft	= MC2DTC / MC2DMD
37	MC2DJ	Polar moment of inertia at midshaft of diaphyseal length MC2	= $\pi/32 * (MC2DMD - MC2DMED)$
38	MC2DZP	Polar section modulus at midshaft of diaphyseal length of MC2	= MC2DJ / (MC2DMD / 2)
39	MC2MMD	MC2 midshaft diameter taken at minimum shaft	Two decimal places
40	MC2MMC	MC2 medial cortex taken at minimum shaft	Two decimal places
41	MC2MLC	MC2 lateral cortex taken at minimum shaft	Two decimal places
42	MC2MMED	MC2 medullary diameter taken at minimum shaft	Two decimal places
43	MC2MTC	MC2 total cortex at minimum shaft	= MC2MMC + MC2MLC
44	MC2MCI	MC2 cortical index at minimum shaft	= MC2MTC / MC2MMD

Field	Variable Name	Variable Description	Comments
45	MC2MJ	Polar moment of inertia at minimum shaft of MC2	$= \pi/32 * (MC2MMD - MC2MMED)$
46	MC2MZP	Polar section modulus at minimum shaft of MC2	$= MC2MJ / (MC2MMD / 2)$
47	MC2MNF	MC2 total diameter at minimum shaft larger than that at the midshaft of the total or the diaphyseal length?	Default is 0; 1 indicates the condition is true
114 -161		Fields 9 to 47 are repeated for the third, fourth and fifth metacarpals	

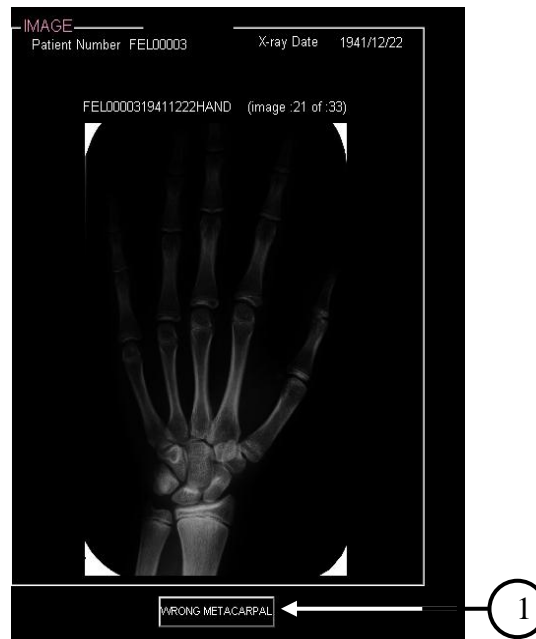


Figure 4.3: Layout of Panel B. If the automated region selection around the metacarpal of interest is incorrect, the user selects the (1) ‘WRONG METACARPAL’ button, which opens a new GUI for manually defining a new metacarpal ROI.



Figure 4.4: GUI for manual metacarpal ROI selection. A rubberband box is drawn around the metacarpal of interest and the medially adjacent metacarpal. This box may be deleted by pressing the (2) 'CLEAR' button. Once the user is satisfied with the selected ROI, pressing the (1) 'SAVE' button stores the ROI coordinates, and returns control to the main GUI. If the metacarpal of interest is not present in the image, the user presses the (3) 'NO METACARPAL' button and then presses (1) 'SAVE' to exit this GUI.

(Figure 4.3, Item 1) located below the image window in Panel B will open a new GUI for manually selecting the region around the metacarpal (Figure 4.4). Once the user is satisfied with the bounding box selection, pressing the 'SAVE' button (Figure 4.4, Item 1) invokes the segmentation algorithm and the automated process continues with recalculation of all values. If the metacarpal of interest is not present in the image, the user selects the 'NO METACARPAL' button (Figure 4.4, Item 2), which results in NaN values being stored in the output file.

4.2.4 Correction for Wrong Approximate Length of the Metacarpal

The GUI also allows for corrections of the approximate metacarpal length assessment, which is subsequently used to calculate the metacarpal orientation. To adjust the automatically determined approximate length, the analyst selects the 'INCORRECT'



Figure 4.5 : Layout of Panel C. The ‘INCORRECT’ button, located below the (1) approximate length, (2) total length or (5) the diaphyseal length figure window, is selected if adjustments are necessary. The ‘REJECT’ button located below the (3) total length or (6) diaphyseal length figure window is selected to reject either of these lengths if the length is not applicable. The (4) ‘DIAPHYSEAL NOT TOTAL’ AutoFix button replaces the diaphyseal length with the total length and deletes the total length whereas the (7) ‘TOTAL NOT DIAPHYSEAL’ AutoFix button replaces the total length with the diaphyseal length and deletes the diaphyseal length.

button (Figure 4.5, Item 1) located below the ‘Approximate Length’ window, which will open a new GUI (Figure 4.6). Within this new window, the user can adjust the endpoints of the initial length estimate line by dragging them to the correct location(s) (Figure 4.6, Item 1). Pressing ‘SAVE’ passes this information to the main GUI, which re-initiates metacarpal segmentation using the updated information and, the automated process continues with recalculation of all subsequent values.

4.2.5 Correction of Metacarpal Total Length

If the total length (actual length, not length estimate) is incorrect, the user selects the ‘INCORRECT’ button (Figure 4.5, Item 2) located below the ‘Total Length’ window,



Figure 4.6: GUI to manually adjust the approximate length. The user clicks on the most distal end of the metacarpal and then drags the mouse to the most proximal end of the metacarpal to draw the approximate length line. Once the user is satisfied with the manually adjusted approximate length line, pressing (1) the ‘SAVE’ button updates the values and returns the user to the main GUI. (2) The ‘CLEAR’ button deletes the manually drawn line.

which will open a new window for manually correcting the total length (Figure 4.7, Item 1). After adjustment of the total length line endpoints, pressing ‘SAVE’ passes the new length to the main GUI, and all subsequent calculations are updated. In cases for which a total length measurement is not appropriate (for example, in young children total length is not defined if the epiphysis is not yet calcified), the user can delete the total length measurement by selecting the AutoFix ‘REJECT’ button (Figure 4.5, Item 3) located below the ‘Total Length’ window. If the automated analysis labels the diaphyseal length as the total length, pressing the AutoFix ‘DIAPHYSEAL NOT TOTAL’ button (Figure 4.5, Item 4) will replace the diaphyseal length with the total length and will delete the total length measurement. This information is passed to the main GUI, and processing continues with updated calculations.



Figure 4.7 : GUI to manually adjust the total length. The auto generated line is initially displayed along the long axis of the metacarpal (since it is difficult for the user to position the line along the exact bone midline), and the user simply adjusts the endpoints of this line as needed. Once satisfied with the manual adjustment, pressing (1) the ‘SAVE’ button updates the values and returns the user to the main GUI. The user also has the option to clear the total length line by selecting (2) the ‘CLEAR’ button.

4.2.6 Correction of Incorrect Metacarpal Diaphyseal Length

As with total length, incorrect diaphyseal length adjustment is initiated by selection of the ‘INCORRECT’ button (Figure 4.5 5) located below the ‘Diaphyseal Length’ window. Within the new window (Figure 4.8), the user can adjust the diaphyseal length. The user can also select the ‘REJECT’ button (Figure 4.5, Item 6) to delete the diaphyseal length in cases for which this measurement does not apply (i.e., post-fusion). Selecting the ‘TOTAL NOT DIAPHYSEAL’ (Figure 4.5, Item 7) AutoFix button will replace the total length with diaphyseal length and delete the diaphyseal length. Processing continues using the updated information.



Figure 4.8: GUI to manually adjust the diaphyseal length. (1) As with the total length, the auto generated line is initially displayed along the long axis of the metacarpal, and the user simply adjusts the endpoints of this line as needed. Once the user is satisfied, pressing (1) the ‘SAVE’ button updates the values and returns the user to the main GUI; pressing (2) the ‘CLEAR’ button deletes the line.

4.2.7 Correction of Incorrect Cortical Thickness Measurements

To correct automatically calculated cortical thickness values (at any of the three locations), the user first selects the ‘INCORRECT’ (Figure 4.9 Item 1) button located below the ‘Thickness’ window in PANEL D. A new GUI (Figure 4.10) is displayed, in which radio buttons allow the user to select the particular location for adjustment of the cortical values (Figure 4.10, Item 1). Next, the user selects the ‘Edit Line Profile’ (Figure 4.10, Item 2) button. A new screen appears that displays the line profile at the selected position; the four automatically determined edge positions (two periosteal and two endosteal edges) are shown as points on the line profile (Figure 4.11, Item 1). The zoomed-in grayscale metacarpal image is also shown with the total and medullary widths (diameters) indicated by colored lines (Figure 4.11, Item 2). The user can select the edge

to be corrected by clicking on the corresponding line profile point and making changes to the location of that point using the left and right arrow buttons located below the line profile plot (Figure 4.11, Item 3). These changes are simultaneously used to update the width of the line displayed in the grayscale image so that the user has immediate feedback about their adjustments. Any changes made in the edge locations can be stored by selecting the 'SAVE' button (Figure 4.11, Item 4), or the user may continue by saving the updated edge locations and then selecting a different edge on the line profile for manual adjustment. At any time the user can reset the edge locations to their original automatically-found values by selecting the 'Reset' button (Figure 4.11, Item 5). Alternatively, the user can execute the 'SAVE and BACK' button (Figure 4.11, Item 6) which returns the user to the main correction screen to select a different location on the metacarpal. After all corrections are made, selecting the 'SAVE' button (Figure 4.11, Item 3) on the selection screen returns control to the main GUI. An additional AutoFix button is provided to correct a problem that arises with the automatic selection of the periosteal edges in the line profile. For most images, an edge-gradient threshold of 70% is successful for selecting the point on the line profile that corresponds to the periosteal edge. However, in some images that threshold must be substantially reduced to find the edge. This occurs when lines have been drawn on the image, but it also occurs in some images without any visible markings. Here, it seems that the overall shape of the metacarpal may be responsible for this problem, and it is reasonable to hypothesize that a non-circular metacarpal might require a lower threshold. Selection of an AutoFix button ("Recalculate Total," "Recalculate Diaphyseal," "Recalculate Minimum Shaft," (Figure 4.10, Items 4-6)) in the 'Thickness GUI' window for each of the three positions invokes a

new edge gradient threshold of 35%. Usually the correct periosteal edge is found with the adjusted threshold even if the gradient between other point pairs in the line profile is much higher than along the actual periosteal edge.

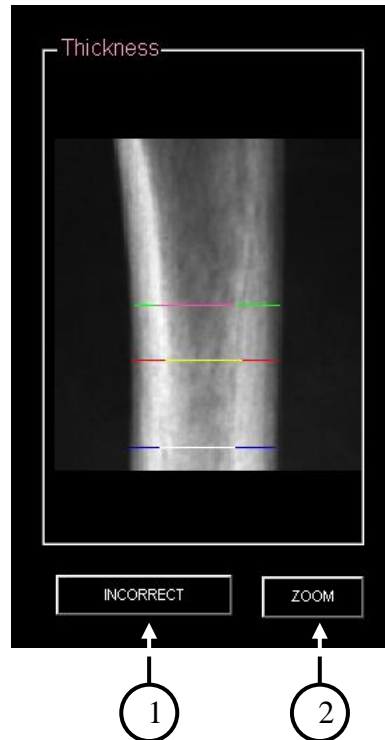


Figure 4.9. Layout of Panel D. The automatically generated cortical and medullary widths are indicated by colored line segments in the figure window. If any width needs to be manually adjusted, selecting (1) the 'INCORRECT' button opens a new GUI for this purpose. Pressing (2) the 'ZOOM' button zooms in on the metacarpal image.

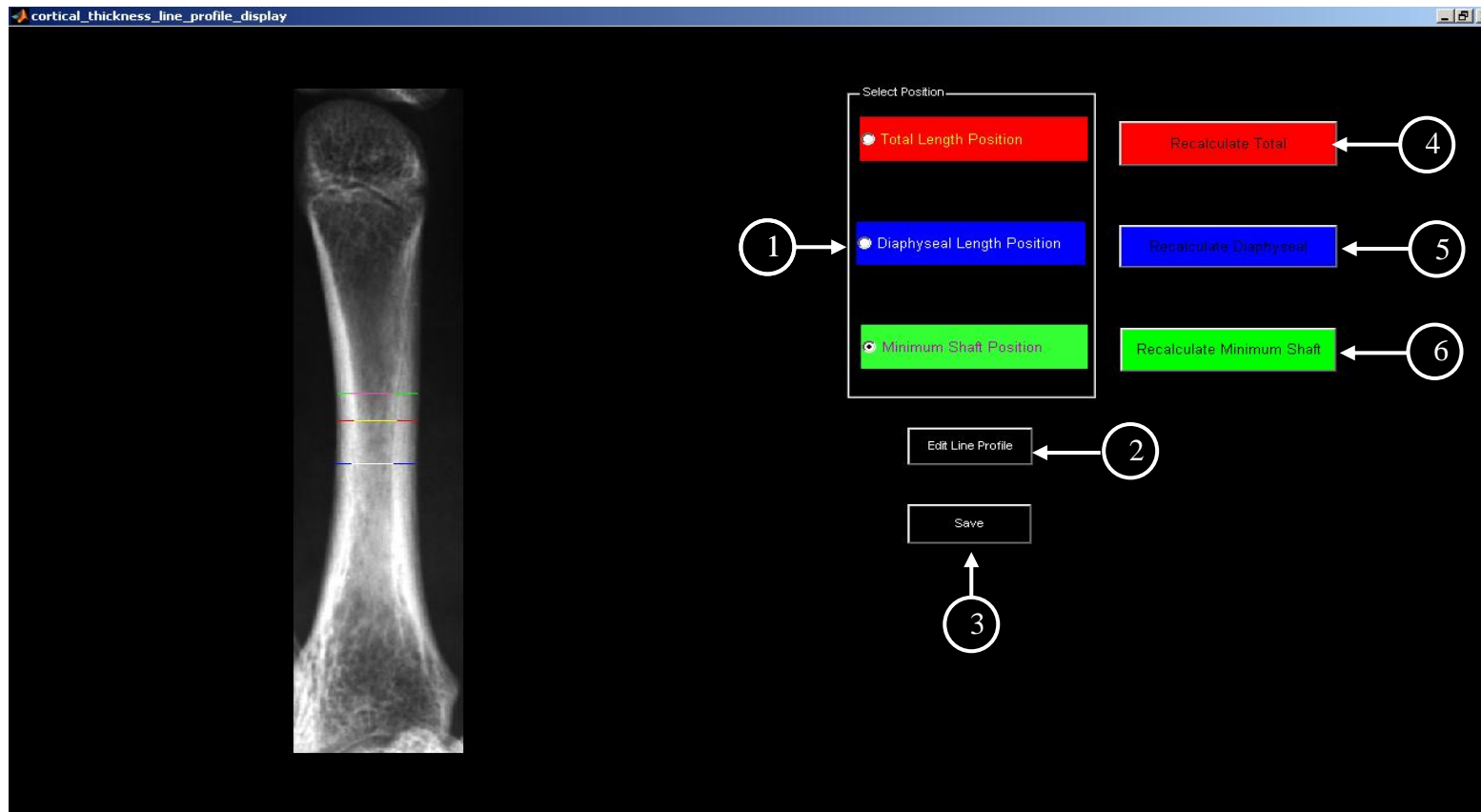


Figure 4.10. GUI for adjustment of automatically calculated cortical thickness values. The user first selects (1) the location, at which the thickness calculations are to be adjusted and then selects the (2) 'Edit Line Profile' button which opens a new line profile GUI. After making all adjustments via the line profile GUI, pressing the (3) 'Save' button updates the stored data and returns the user to the main GUI. Three AutoFix buttons (4-6) are available (one for each location) that, when selected, modify the edge selection criteria and recalculate the cortical thickness at that location.

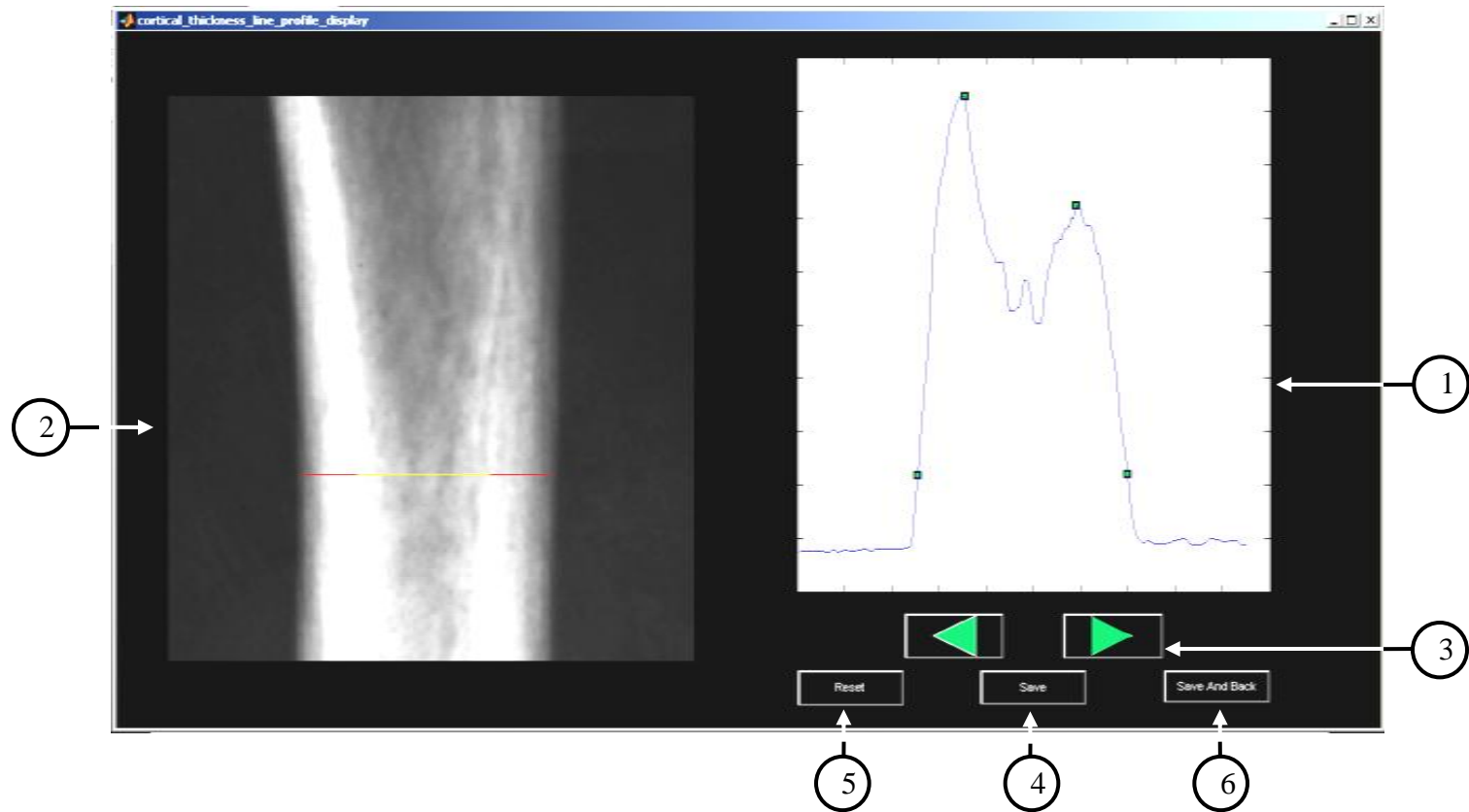


Figure 4.11. Line profile GUI for adjusting cortical width measurements. The GUI displays (1) the line profile at (2) the selected metacarpal position. The lengths of the colored line segments (representing cortical thickness and medullary cavity thickness) are adjusted when the user updates the edge points on the line profile. After selecting the green marker corresponding to the edge that needs to be corrected, the user can update the edge position either toward or away from the bone midline using (3) the arrow buttons. Pressing the (4) 'Save' button stores the current edge locations and allows the user to adjust another edge position. At any time, the user can reset the edge locations to their original, automatically found values by selecting the (5) 'Reset' button. When all adjustments are satisfactory, pressing the (6) 'Save And Back' button returns the user to the Thickness GUI.

5. RESULTS

5.1 Edge Corrections

The sigma for the blurring function of the system was found to be 1.65. This sigma yielded a correlation value (R) of 0.9983 between the experimentally measured edge and the blurred ideal edge. By applying this blurring function to the simulated metacarpal line profile and comparing the original and blurred profiles, we found that the shift in the peak location corresponding to the endosteal edge was one pixel toward the midline of the bone (Figure 5.1). Comparing the positions of the maximum gradient in the two line profiles yielded the shift in the location of the periosteal edge. This shift due to blurring was found to be one pixel in the outer direction (toward soft tissue) (Figure 5.1). To summarize the edge corrections, the total number of edge adjustment pixels by edge is provided in Table 5.1. These corrections are applied within the software to the edges found either automatically or manually.

5.2 Cortical Width Plot

To illustrate the output of the analysis procedures, the total cortical width TC at the minimum shaft location for a single participant is plotted as a function of the year in which the radiograph was acquired (Figure 5.2). Recall that the participant's age at the

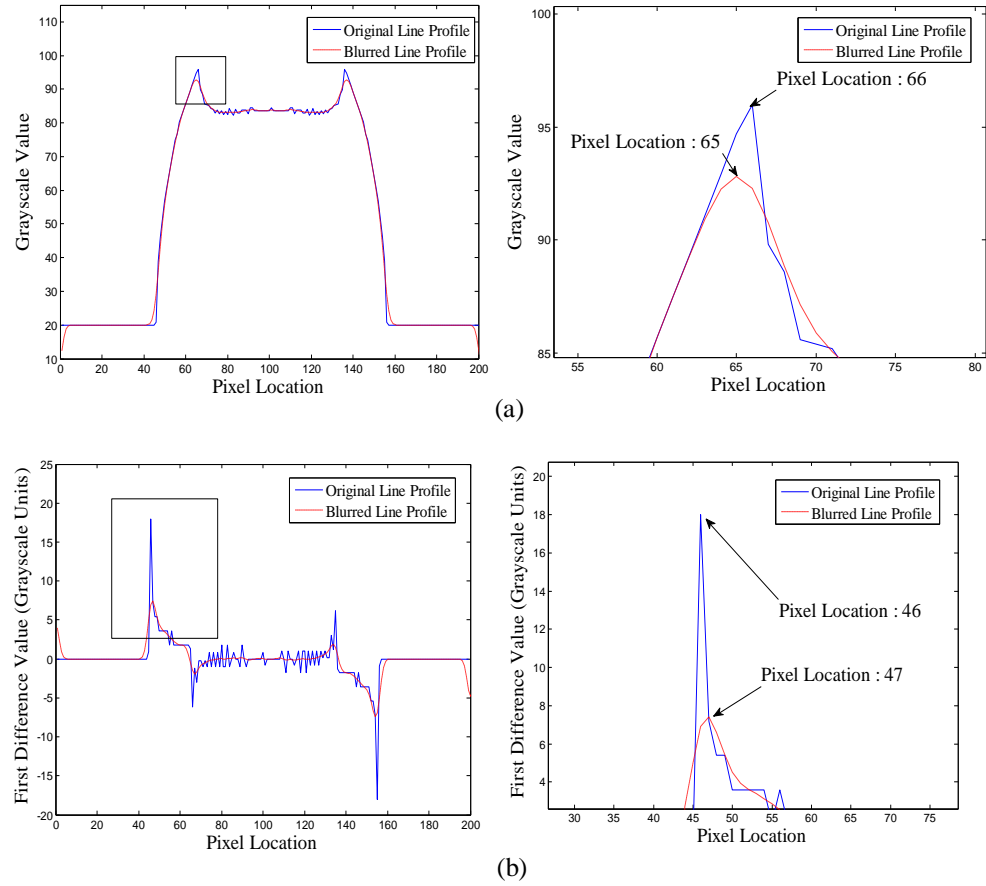


Figure 5.1. To find the shift in the location of the metacarpal edges due to system blur, a simulated line profile across the metacarpal was convolved with the blurring function of the system. For the medial edge, a) the shift in the peak location (corresponding to the endosteal edge) was one pixel in the outward direction (seen more clearly on the right) and b) the shift in the maximum gradient in the first difference (corresponding to the periosteal edge) was one pixel in the inward direction (seen more clearly on the right).

Table 5.1: Edge corrections due to blur and finite pixel size are invoked on the automatically found edge locations. Effects at the periosteal and endosteal edges are different and are shown here for both the medial and lateral cortices. The signed values represent the number of pixels to be added to the automatically or manually found edge locations. The corrections take place within the software routines.

	Medial		Lateral	
	Periosteal	Endosteal	Endosteal	Periosteal
Blur Factor	-1	+1	-1	+1
Half Pixel Shift	-0.5	+0.5	-0.5	+0.5
TOTAL	-1.5	1.5	-1.5	1.5

time of image acquisition is not stored in the filename and is, thus, unavailable within the program. However, the time interval between the radiographs corresponds to the difference in age between subsequent visits, and a trained analyst can estimate the participant's age at the first radiograph. Subsequent images can then be associated with an age based on this references value, and the participant's *TC* value over time can be compared to the expected trend of a normal individual. As one would expect, *TC* increases rapidly until adolescence, peaking in early adulthood, and then decreases with age. Program output at specific time points throughout that participant's lifespan show the anatomical variation with age (Figure 5.2, Figure 5.3, Table 5.2).

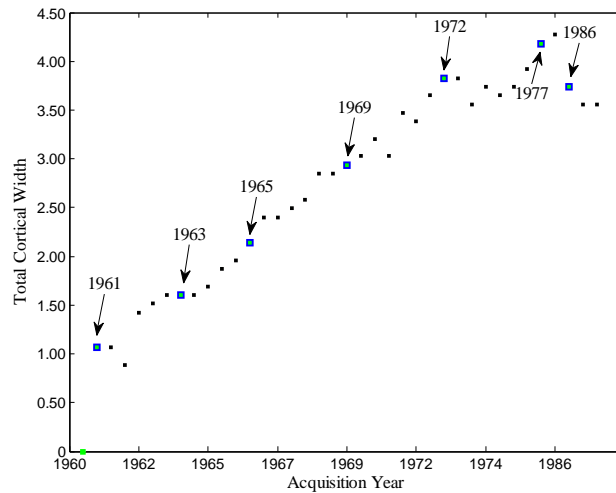


Figure 5.2. Plot showing the typical variation in the total cortical width as a function of age, throughout the lifespan. These data are for the participant whose hand-wrist radiographs are shown in Figure 5.3 (the highlighted points here correspond to the provided hand and metacarpal images) with the horizontal axis tick marks labeling every fifth visit.

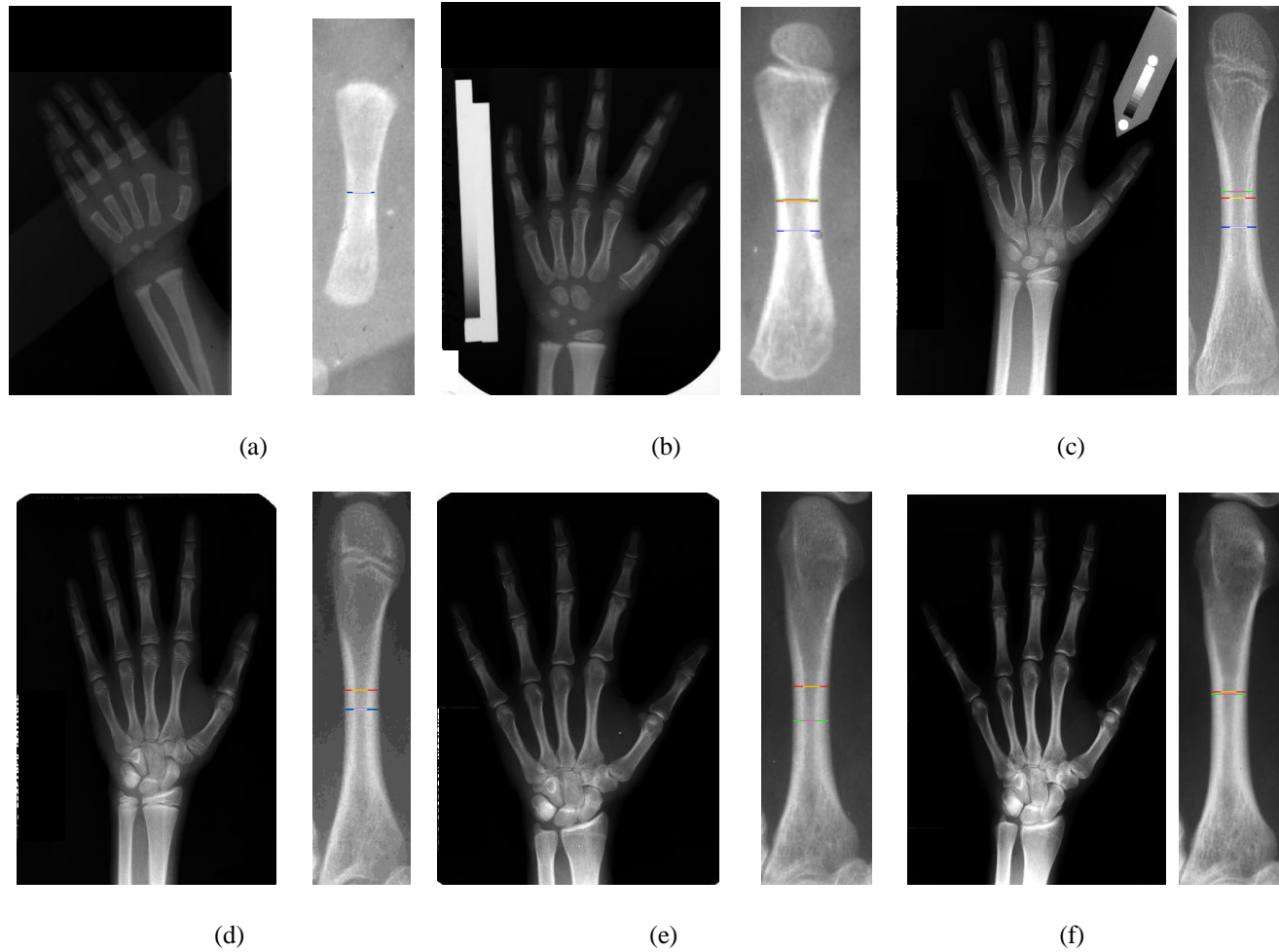


Figure 5.3 Variation in the anatomy as a function of age of the participant whose growth data are plotted in Figure 5.2. For each highlighted point on that plot, the corresponding hand-wrist radiograph and the segmented and rotated metacarpal is shown. Metacarpal cortical thickness is marked at the midshaft of the total length, midshaft of the diaphyseal length and at the position of minimum shaft width.

Table 5.2 The parameters of interest measured across the second metacarpal corresponding to the participant images in Figure 5.3(a-f). N/A = not applicable.

Figure Number	Year of Image Acquisition	Total Length <i>TL</i> [mm]	Diaphyseal Length <i>DL</i> [mm]	Medullary Diameter <i>MD</i> [mm]	Medial Cortex <i>MC</i> [mm]	Lateral Cortex <i>LC</i> [mm]	Total Cortex <i>TC</i> [mm]	Total Diameter <i>TD</i> [mm]	Cortical Index <i>CI</i>
5.3a	1961	N/A	21.72	1.78	0.89	0.79	1.60	3.38	0.473373
5.3b	1963	37.38	31.24	2.58	0.98	1.16	2.14	4.72	0.453390
5.3c	1969	51.98	43.79	2.49	1.78	1.69	3.47	5.96	0.582215
5.3d	1972	63.37	56.60	2.49	1.96	2.40	4.36	6.85	0.636496
5.3e	1977	71.65	N/A	2.58	2.14	2.58	4.72	7.30	0.646575
5.3f	1986	71.82	N/A	3.03	2.14	2.14	4.28	7.30	0.586301

5.3 Success of Automated Analysis

Algorithm success was evaluated by running the automated analysis on 357 hand-wrist images (from the available data set of 17,000 images), the output of which were analyzed by two well trained image analysts from the FLS. Since image quality directly impacts the success of the automated analysis, the images were first classified into two groups: Group 1 is comprised of images of reasonable quality; images in Group 2 (Figure 5.4-5.6) exhibit poor quality due to very low contrast (60.4%), presence of a substantial portion of the radius and ulna (6.3%), a high degree of hand rotation (7.9%), marks across metacarpals (19.0%), etc (6.3%) (Figures 5.4 and 5.5). Images in Group 2 are likely to require user intervention.

Within Group 1, automated analysis was defined to be successful if no manual intervention was needed, if the analyst used the auto fix button(s) or if only limited manual intervention was necessary (i.e., slightly extending a calculated metacarpal length

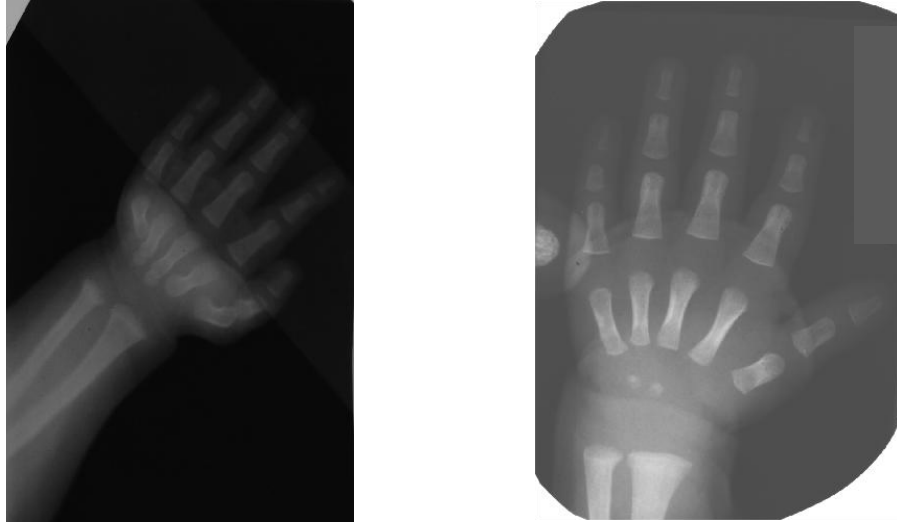


Figure 5.4. In some images, spatula-like devices were used to flatten infant's hands to better visualize the metacarpals. Depending on how the holding device affected image quality, these images may be classified into either Group 1 or Group 2.



(a)



(b)

Figure 5.5. These are examples of images that were classified into Group 2. a) An underexposed image yields poor bone-edge definition and finding the endosteal edges proves difficult. b) A severely overexposed image is also problematic. Both automated analysis and manual analysis failed in each of these cases.

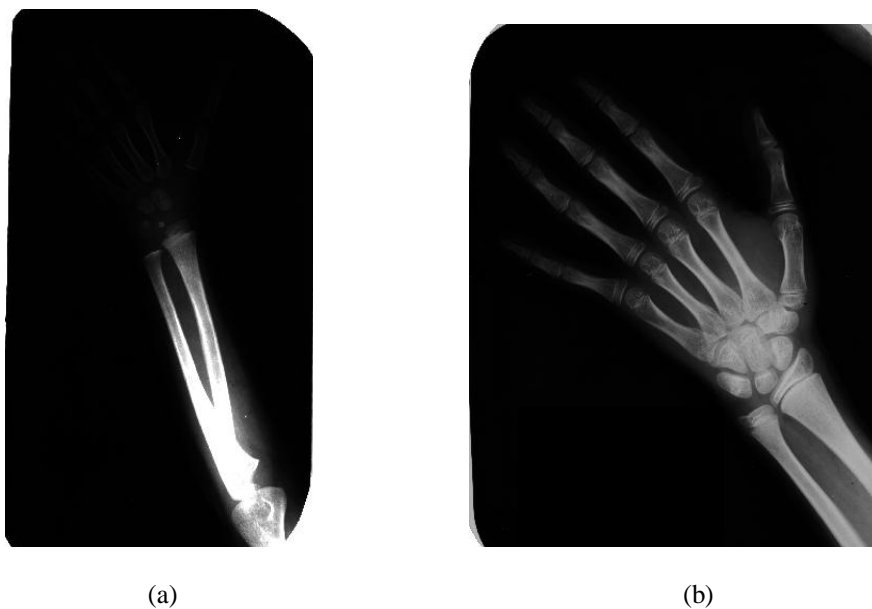


Figure 5.6. These Group 2 images exhibit a) a substantial portion of the forearm (radius and ulna) in the image, and b) a high degree of hand rotation, resulting in the failure of automated analysis routines. In each of these cases, manual analysis also failed.

line). This characterization is consistent with the analysts' (our clients) definition of success.

Apart from issues that can be resolved using the AutoFix tools or other limited manual intervention, auto analysis failed for Group 1 and 2 images when 1) the correct metacarpal of interest is not automatically selected initially; or 2) the values for the endosteal or the periosteal edges are incorrect and cannot be corrected through the AutoFix mechanism. The outcomes of each of these two cases can be further subdivided based on whether the user was able to obtain correct measurement values after more substantial manual intervention. The overall software success is reported here by tallying the number of tested images within each group that fall into the three outcome groups: automatic success (includes limited manual intervention), success after manual intervention and unsuccessful (Figure 5.7). Two values for the success percentage at each

step are given; the first value is the percent success from all images in the preceding step and the second value (in curly brackets) is the fraction of all analyzed images successful at that stage.

5.4 Interobserver Agreement and Reliability

One anticipated benefit of automated image analysis is improvement in measurement precision. To analyze the reproducibility and the agreement of the developed algorithm, the interobserver agreement, which is the degree of agreement between multiple observers viewing the same event, object or phenomenon,²⁵ was tested using the following definition:

$$\text{Interobserver Agreement} = \frac{n_a}{n_o} 100, \quad [5.1]$$

where n_a corresponds to the number of agreements and n_o corresponds to the number of opportunities to agree.

The 357 images analyzed to assess the overall algorithm success were used to gauge interobserver agreement. Two observers (the trained FLS image analysts) analyzed those images and the generated data (Excel output files) were compiled for this task. To examine interobserver agreement, the total cortical width TC at the minimum shaft location was selected as the measurement of interest (this is a major variable of interest in the overarching study and is the value reported graphically within the GUI). The definition of “agreement” was set by our client as follows: “two measures are in agreement if they lie within 0.5 mm of each other.” This physical measurement is equivalent to approximately five pixels. In the event that one of the analysts was able to

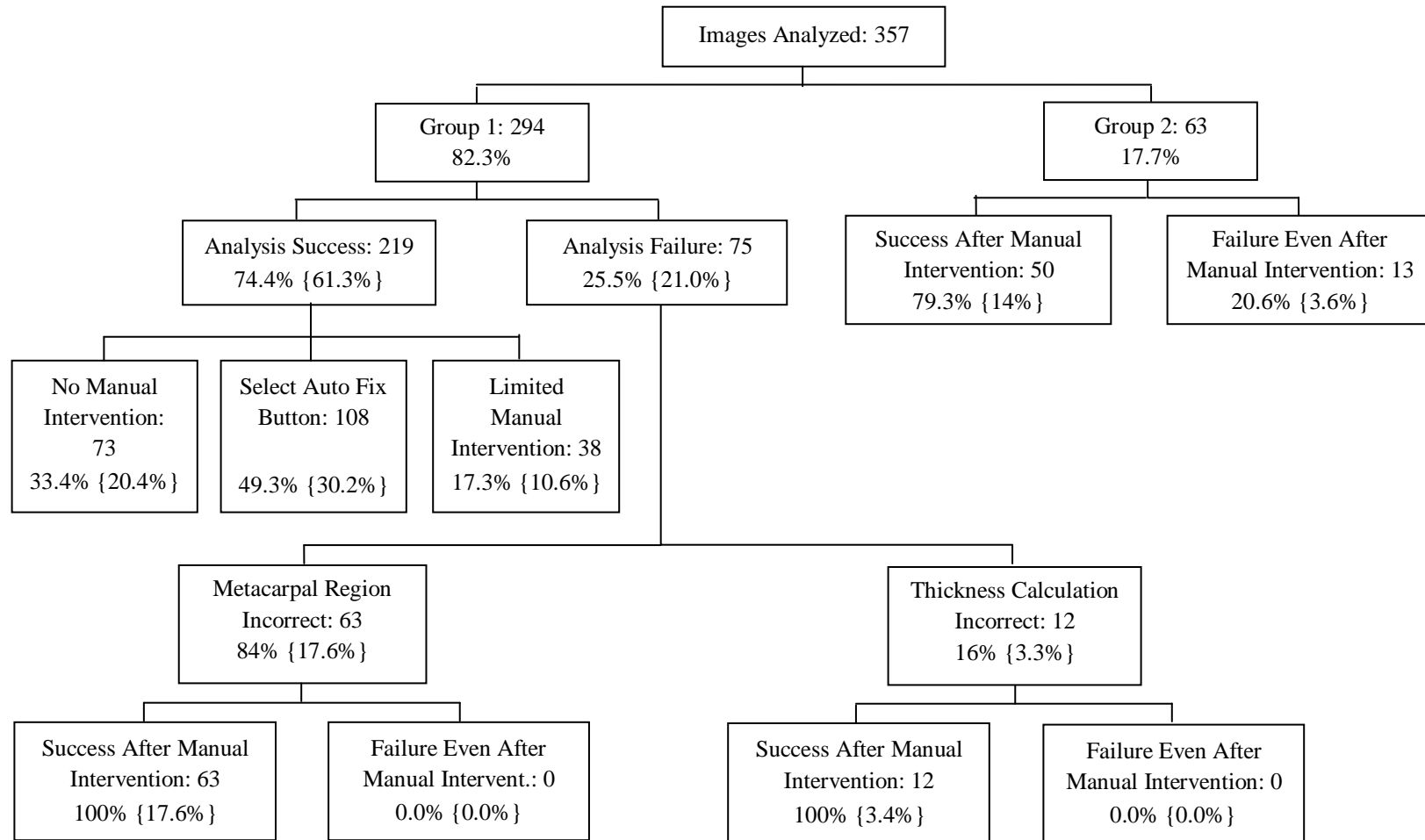


Figure 5.7. Results of the automated analysis routines. At each step the number of images in that category are given, along with two values for the success percentage; the first value is the percent success from all images in the preceding step and the second value (in curly brackets) is the fraction successful from all 357 analyzed images.

analyze the image but the other selected ‘No Analysis’, or if both selected ‘No Analysis’, then the difference between the *TC* values from the two analysts cannot be calculated and these images were excluded from the interobserver agreement analysis. Of the 316 images retained, measurements of 297 images were in agreement, yielding an interobserver agreement of 92.08%.

To assess interobserver reliability, the Pearson correlation coefficient and the mean of the absolute difference of the measurements by the two observers were calculated. The correlation coefficient (*r*) and mean were 0.9674 and 0.1793 mm, respectively.

5.5 Intraobserver Agreement and Reliability

Intraobserver reliability indicates the stability of given responses obtained from the same respondent at different times.²⁶ To assess intraobserver reliability, a set of 30 images was analyzed twice. The entire set was analyzed once before repeating the analyses the second time, approximately 8 days later. Similar to the interobserver study, the total cortical width values at the position of minimum shaft width were extracted from the output files and compared for agreement. Here, we defined agreement as *TC* values within 0.267 mm of each other (corresponding to 3 pixels). Intraobserver agreement is defined as

$$\text{Intraobserver Agreement} = \frac{n_a}{n_o} 100, \quad [5.2]$$

where n_a corresponds to the number of agreements and n_o corresponds to the number of opportunities to agree. Of the 30 images analyzed, 29 were in agreement, yielding an intraobserver agreement of 96.7%.

To assess intraobserver reliability, the Pearson correlation coefficient and the mean of the absolute difference between the measurements by a single analyst were calculated. The correlation coefficient (r) and mean were 0.9929 and 0.0506 mm, respectively.

5.6 Comparison of Manual versus Automated Measurement Reliability

The interobserver and the intraobserver agreements of the automated method were compared to those from manual analysis using digital calipers (Table 5.3). For the manual analysis reliability studies, the interobserver agreement was assessed using 20 images and the intraobserver agreement was assessed using 16 images. For the automatic analysis assessment, the output files generated in the reliability analysis were compiled and the actual measurement values were compared.

Table 5.3: Comparison of interobserver and intraobserver agreement for the manual and automated analyses of total metacarpal cortical thickness at the position of minimum shaft width.

	Manual Analysis		Automated Analysis	
	Interobserver Agreement	Intraobserver Agreement	Interobserver Agreement	Intraobserver Agreement
# of Images Analyzed	20	16	316	30
Agreement Threshold [mm]	0.500	0.267	0.500	0.267
Percentage in Agreement	50.00%	50.00%	92.08%	96.70%

The correlation r was much higher for the automated versus the manual analysis: the interobserver study yielded a correlation value of 0.9674 versus 0.7000, and the values for the intraobserver study were 0.9929 versus 0.7820.

Table 5.4: Comparison of interobserver and intraobserver reliability for the manual and automated analyses of total metacarpal cortical thickness at the position of minimum second metacarpal shaft width.

	Manual Analysis		Automated Analysis	
	Interobserver	Intraobserver	Interobserver	Intraobserver
Correlation Value (r)	0.7000	0.7820	0.9674	0.9929
Mean [mm]	0.6420	0.3568	0.1793	0.0506

6. DISCUSSION

We have developed a tool for analyzing metacarpal thickness from hand-wrist radiographs. Testing the software on a set of approximately 360 images revealed that the program was successful in automatically analyzing images (including poor quality images) about 75% of the time with no more than limited manual intervention. The remaining images were classified by the analyst as being of reasonable or poor quality. Of these reasonable quality images, 100% were able to be analyzed by the analyst. The 60 poor-quality images required user intervention. Of this group, 79.3% were able to be analyzed using user intervention, and the remaining 20.7% could not be analyzed (even with manual intervention).

Since the automated analysis gave high interobserver and intraobserver reliability values, we can conclude that the program is largely independent of user intervention and would generally arrive at the same output, even if the user(s) manual corrections are not exactly identical. Also minimal training was required to use this software successfully. Although the users in the reliability tests were trained, they had not used the program extensively before the reliability studies.

Our software was customized to the client's needs, using feedback received from them during the development process. Compared to commercially-available software, we have

provided a product that can be modified as needed if new measurement requirements are identified or if changes to the layout are desired.

6.1 Challenges in Automated Image Analysis

Thresholding and Segmentation Issues

Automatic thresholding to first segment the hand and then the metacarpals is challenging because of image variability. Differences in anatomy and degree of mineralization across the age range of FLS participants impacts image contrast. Additional variability due to film quality affects the success of our automated routines. We attempted to mitigate the issues related to image quality by customization of the pre-processing phase based on a particular image's overall contrast. Still, the degree of mineralization in a given image will directly affect contrast and can make segmentation of the metacarpal region of interest difficult, since mineralization varies across participants and also across a single participant with age.

The method relies on *a-priori* information about the anatomy of the hand, but that anatomy is variable across the participant's lifespan. At an early age, the metacarpals and carpals are well separated, but over time, the metacarpal and the carpals begin to overlap and, in adulthood, distinguishing the boundaries is impossible at times. In these cases, portions of the carpal region are also included in the output of the metacarpal segmentation process, and this affects the length estimate. To more accurately find the inclination, even when the length estimate is off by several pixels, the rows selected along the middle half of the length estimate while calculating the angle were rejected as follows. First, the mean column value of all included rows was calculated. If the mean

value of any row, proceeding distally-to-proximally, exceeded this value by 25%, the rows below it were excluded from the inclination angle calculation. This yielded an accurate orientation calculation even if only a small portion of the carpal region was included. To avoid errors in the total length calculation when metacarpal segmentation was grossly inaccurate, two length criteria were checked. If the total length was greater than 850 pixels, the lower 5% of pixels were excluded and if the total length value was greater than 950, then the lower 10% of pixels were excluded. The total length was then recalculated.

Film quality variation was the most important factor leading to failure in thresholding even after applying appropriate pre-processing steps. This is because the overall histogram shape changes with image quality. Pixels of an overexposed film lie in the lower histogram regions and occupy a very small portion of the overall dynamic range, whereas an underexposed film's histogram shows its pixels occupying a very small region in the upper portion of the available dynamic range. In overexposed radiographs, the threshold value obtained from Otsu's method (which relies on the image histogram) tends to over-segment (turn off pixels even within the object) the hand and metacarpal regions, whereas unwanted background regions are included after segmentation of underexposed radiographs (under-segmentation).

Since the algorithm is divided into steps and each step is dependent on the success of the previous step, failure at any stage is propagated and usually leads to failure of the subsequent steps.

Selecting the ROI for the Second Metacarpal

Hand anatomy also plays an important role in metacarpal ROI selection. Here, accurate information about the location of the peaks corresponding to each metacarpal is required, but in some participants the inclination of the thumb metacarpal makes it difficult to obtain the five peaks across any row. Further, since the soft-tissue thickness is usually greater between the thumb and the second metacarpal than between the other metacarpals, the segmentation step may result in the thumb being separated from the rest of the hand. In these cases, the thumb will be eliminated when the largest object in the image is retained. This issue led to our approach in counting peaks from the left (medial) side of the image and checking to see if five peaks exist in a row. When no image row contained five peaks, rows having four peaks were selected instead and it was assumed that these corresponded to the second to fifth metacarpal (excluding the thumb). However, in some four peak cases it was the fifth metacarpal, rather than the thumb, that was missing. This was caused by a different thresholding issue, and relates to the small size and, therefore, low grayscale values within the fifth metacarpal. In this event, the program incorrectly labeled the thumb as the second metacarpal (fourth peak from the left). To avoid this error if four peaks were present, the inter-peak distances and the heights of the peaks were calculated and used to label the third peak as the second metacarpal. Still there are cases wherein the method was not successful. When less than four peaks were present, we used the most probable case (second to fourth metacarpals are present) to label the structures. The method to find the location of the second metacarpal is further complicated if the hand is rotated, since the calculations of the inter-peak distances and the heights of the peaks are not reliable.

Imaging protocol changes could have a major impact on the quality of the radiographs obtained. It is understandable that a fixed set of imaging parameters is desirable for such a study. Further, the study protocol has been adapted to accommodate new x-ray tubes and film types. Based on film analysis, we propose that at least two sets of exposure conditions should be specified in the protocol: one set for children and one set for adults. If the settings were adjusted based on participant size (age) there would be fewer cases of overexposure in images of children and fewer cases of underexposure in adults. Also by keeping the hand consistently aligned with the film's axes, several failures in segmenting the second metacarpal ROI would likely be avoided.

6.2 Total Cortical Width Plot

The plot of the total cortical width displayed in the GUI serves several functions. Apart from verifying whether a particular participant follows the typical trend, this plot also allows the analysts to easily spot outlier points. Since the trend of cortical width, as well as the expected maximum deviation away from this trend line, is known to the trained analyst, it is likely that the automatic analysis has failed if a point falls outside these limits. The analyst should review that image carefully. Further, the software can also recognize that it has failed and is unable to generate meaningful output; in those cases, the cortical width is set to zero and that image point is obvious in the plot. Lastly, when an image is marked as 'No Analysis' possible, cortical thickness is also set to zero. To distinguish between the latter two cases, the "automatic analysis failed" zero points are displayed in red, whereas the "No Analysis possible" zero points are displayed in green. Red data points are flags that indicate the need for additional manual intervention.

6.3 Other Approaches Investigated

As with most image processing tasks, several approaches were tested at each step, and the most reliable method was retained in the final version of the software. Here, we will describe a few techniques that were tested and subsequently abandoned.

Skeletonization

Initially, to find the ROI around the second metacarpal region, the skeleton of the binary image was formed by eroding the image without letting objects break apart and vanish. A skeleton is one pixel thick, and it always passes through the center of an object, while preserving the object's shape or topology. The obtained skeleton is usually very noisy, because it is a function of the shape of the object and non-uniformity generates additional branches in its skeleton. In this project, it was difficult to find the location of the second metacarpal from the skeleton of the hand because of the many branches that existed. We needed more information to obtain the location of the second metacarpal. The images' EDM provided a more complete picture of the hand shape and thickness, since the main structure and branches are distinguished by differing grayscale values.

Periosteal Edge Selection

Initially, to find the periosteal and the endosteal edges, we found the roof and the floor along the line profile taken horizontally across the metacarpal at the location of interest. The method assumed a perfect edge such that the edge lies exactly in the center of the roof and the floor. Depending upon the imager's blurring function, the slope of the line connecting the floor and the roof changes and the number of pixels required to reach the roof from the floor changes. The position of the edge sits at the value corresponding to

floor + some fraction of the distance between the floor and the roof. In an ideal profile, that fraction would be 50%, but in the blurred profile, this fraction must be determined experimentally. We first found this percentage value from the images of the step-wedge imaged using the FLS x-ray system. Using the known step wedge width, we adjusted the fraction until the corrected image width matched the wedge width and noted the final fraction required in that case. However, we later realized that this method is only accurate when the object being imaged is a perfect slab. In our case, the geometry was quite different, so a different approach to finding the blur correction was needed. In the case of a circular object like a metacarpal, the transition from the floor to the peak will depend on the radius of the metacarpal, the thickness of the cortex as well as the blurring factor. Material inhomogeneities also impact the shape of the line profile, but we assumed a homogeneous cortex. The method used in the actual automation process to find the periosteal and the endosteal edge was confirmed by simulating circular objects and then finding the pixel location in the line profile corresponding to actual edge location. This simulation method can be used even for non-circular objects if the object shape can be reasonably estimated.

6.4 Future Work

More accurately labeling the diaphyseal and total lengths

Currently there are AutoFix buttons present to replace the diaphyseal length with total length, or total length with diaphyseal length. In infants, no total length is present since the epiphysis is not yet calcified, but the program finds the total length first and the diaphyseal length is mislabeled as total length. The ‘DIAPHYSEAL NOT TOTAL’ button is used more often than the ‘TOTAL NOT DIAPHYSEAL’ button. Although the

AutoFix button readily corrects this issue, a method to automatically and correctly label each length would be preferred. A proposed method would be to find a length threshold for the total length and label any length below this length as a diaphyseal length. Since only infant radiographs are mislabeled, the metacarpal length in these cases is small. To implement this requires a careful analysis of a sufficient number of metacarpal lengths over all age ranges; it may be necessary to determine a metacarpal-specific threshold if there are appreciable differences in the lengths of the second, third, fourth and/or fifth metacarpals.

Improvement in finding lengths

Active Shape Models (ASM) are used in a lot of computer vision based projects and their application is potentially useful for metacarpal segmentation in this project. ASMs are defined by points on the boundary of the shape that is to be reconstructed.²⁷ The algorithm needs to be trained by placing the points manually on a set of training images and then constructing a model from it. Since we were more interested in taking measurements at specific metacarpal locations, rather than precisely defining the contour around the metacarpal, we did not explore the use of ASMs. Also the learning curve for ASM is steep, and the project had to be completed in a set time period.

The major advantage of a well-trained ASM would have been the ability to segment the metacarpal and the carpals even when there is no clear separation between them, because the approach is based on *a-priori* information about the shape of each metacarpal. Apart from accurate calculation of the lengths, the ASM could also be used for accurate calculations of the periosteal edges because it should return a smooth outer contour of the

metacarpal. One disadvantage of ASMs is the need for a seed point inside the object and often that is accomplished through manual intervention. Our method does not require this initiation. If an ASM approach is ever implemented in the future, our software could be used for identifying this seed point automatically inside the metacarpal.

Reducing the time required for analysis

The average time required to automatically analyze each image is approximately four minutes, with the infant hands being completed in approximately one to two minutes and an adult hand in four to five minutes. Since a typical participant's folder of images contains, on average, about 25 images, the analysis of an entire set of images from a single participant requires approximately 100 minutes. Analysis is usually done overnight, and at least 8 subjects can be analyzed per night (more over a weekend) on a single workstation, which is then available for regular use during the workday. Review of the results requires approximately 25 minutes per participant folder, including manual correction of results. In contrast, it was estimated that the manual analysis of these images using digital calipers would require at least 3 to 5 minutes per image and all radiographs are analyzed twice to obtain accurate manual measurements. Manual analysis of a single participant's folder of images would require about 200 minutes per metacarpal (a time increase of about 87.5% when compared to the time the analyst takes to review the results of the automated analysis (Table 6.1)). Of course, the digitization step required a tremendous number of hours, but that was accomplished while the code was being developed and, to date, almost 80% of the 17,000 radiographs to be analyzed in this study

Table 6.1: Efficiency calculations of the automated analysis process across a patient folder containing an average of 25 folders.

	Manual Analysis	Automated Analysis Review
Each Metacarpal	8 minutes	1 minute
Time/Image (all metacarpals)	32 minutes	4 minutes
Time/Folder	800 minutes	100 minutes

have been digitized. Automated analysis of these images should be completed within three months.

Although efficiency of the software was considered at each step in the algorithm, the need for accurate measurements rather than the speed of execution drove the final implementation of the processes. The code can run faster if the image data are downsampled, so that each of the processing steps is completed faster. Also since we are working with 16 bit images, the time required for any step that involves histogram analysis is relatively long; this could be reduced by carrying out the analysis at a lower grayscale bit depth. In the current implementation, some strategies were employed to minimize repetitive calculations. For example, while carrying out steps like selecting the largest object in the original hand radiograph or finding the metacarpal after watershed segmentation, every tenth row and column were analyzed (rather than every row and column) because an object of interest cannot be less than 10 pixels wide.

Using the present tool to analyze other bones in the hand

Since the shapes of the phalanges and the metacarpals are similar, by using the knowledge about the shape and the position of the bones relative to one another in the hand, this work could be extended to provide a tool for measuring the phalanges. With a little modification of the segmentation code, the software could be used for assessing cortical widths in the phalanges. Using the same GUI, the user could select a region around a region of a phalanx and obtain the variables of interest for this bone. It is likely that the segmentation algorithms would need to be optimized for this task, but the basic modules and tools are available for this analysis. To test if the present tool (without any modifications) could be used for the segmentation of the phalanx, a phalanx ROI was selected instead of the metacarpal ROI, and the analysis was carried out. The phalanx was segmented properly and, with some limited user intervention, appropriate phalangeal measurements were obtained. This simple experiment demonstrated the versatility of the code for other long bone analysis tasks.

6.5 Conclusion

Overall, we feel that the requirements put forward by the client were achieved and that a customized, well tailored product was developed. The software is currently being used successfully at the Lifespan Health Research Center (Department of Community Health, Boonshoft School of Medicine, Wright State University) for analysis of metacarpal cortical thickness in hand radiographs of the FLS participants.

REFERENCES

1. Duren DL, Sherwood RJ, Choh AC, Czerwinski SA, Chumlea WC, Lee M, Sun SS, Demerath EW, Siervogel RM and Towne B (2006) Quantitative genetics of cortical bone mass in healthy 10-year-old-children from the Fels Longitudinal Study. *Bone*, 40, 464-470.
2. Olney RC (2003) Regulation of bones mass by growth hormone. *Medical and Pediatric Oncology*, 41, 228-234. Nguyen TV, Maynard LM, Towne B, Roche AF, Wisemandle W, Li J, Guo SS, Chumlea WC and Siervogel RM (2001) Sex differences in bone mass acquisition during growth. *Journal of Clinical Densitometry*, 4(2), 147-157.
3. Nguyen TV, Maynard LM, Towne B, Roche AF, Wisemandle W, Li J, Guo SS, Chumlea WC, and Siervogel RM (2001) Sex differences in bone mass acquisition during growth. *Journal of Clinical Densitometry*, 4(2), 147-157.
4. Garn SM (1970) *The Earlier Gain and the Later Loss of Cortical Bone*. Charles C Thomas Publisher, Bannerstone House, Springfield, IL, 3-59.
5. Ruimerman R (2005) Modeling and remodeling in bone tissue. Ph.D. Dissertation, University of Technology, Eindhoven, Netherlands.

6. Wilson AN, Schmid MJ, Marx DB and Reinhardt RA (2003) Bone turnover markers in serum and periodontal microenvironments. *Journal of Periodontal Research*, 38, 355-361.
7. Raisz LG and Seeman E (2001) Causes of age-related bone loss and bone fragility: an alternative view. *Journal of Bone and Mineral Research*, 16(11), 1948-1952.
8. Audi L, Ramirez MG and Carrascosa A (1999) Genetic determinants of bone mass. *Hormone Research*, 51(3), 105-123.
9. Heaney RP, Abrams S, Dawson-Hughes B, Looker A, Marcus R, Matkovic V and Weaver C (2000) Peak bone mass. *Osteoporosis International*, 11(12), 985-1009.
10. John DK and Walter PB (1972) Osteogenesis imperfecta: an orthopaedic description and surgical review. Division of Orthopaedic Surgery, Hospital for Sick Children, Toronto.
11. Bonnick SL (2003) *Bone Densitometry in Clinical Practice: Application and Interpretation*. Humana Press, New York, NY, 32.
12. Grampp S, Steiner E and Imhof H (1997) Radiological diagnosis of osteoporosis. *European Journal of Radiology*, 7(2), S11-S19.
13. Barnett E and Nordin BE (1960) The radiological diagnosis of osteoporosis: a new approach. *Clinical Radiology*, 11, 166-174.
14. Crespo R, Revilla M, Usabiago J, Crespo E, Arino JG, Villa LF and Rico H (1998) Metacarpal radiogrammetry by computed radiography in postmenopausal women with Colles' fracture and vertebral crush fracture syndrome. *Calcified Tissue International*, 62, 470-473.

15. Rosholm A, Hyldstrup L, Baeksgaard L, Grunkin M and Thodberg HH (2001) Estimation of bone mineral density by digital x-ray radiogrammetry: theoretical background and clinical testing. *Osteoporosis International*, 12(11), 961-969.
16. Curry TS, Dowdey ED and Murry RC (1990) *Christensen's Physics of Diagnostic Radiology*, Lea & Febiger, Philadelphia.
17. Bottcher J, Pfeil A, Rosholm A, Schafer ML, Malich A, Petrovitch A, Seidl B, Lehmann G, Mentzel H, Hein G, Wolf G and Kaiser WA (2006) Computerized digital imaging techniques provided by digital x-ray radiogrammetry as new diagnostic tool in rheumatoid arthritis. *Journal of Digital Imaging*, 19(3), 279-288.
18. Sotoco JM, Inesta JM and Belmonte MA (2002) Hand bone segmentation in radioabsorptiometry images for computerized bone mass assessment. *Computerized Medical Imaging and Graphics*, 27, 459-467.
19. Garcis LR, Fernandez MM, Arribas JI and Lopez A (2003) A fully automatic algorithm for contour detection of bones in hand radiographs using active contours. *IEEE International Conference on Image Processing*, 3, 421-424.
20. Gonzalez RC and Woods RE (2004) *Digital Image Processing*, Addison-Wesley Publishing Company, Menlo Park, CA, 79-80.
21. Otsu N (1979) A threshold selection method from gray-level histograms. *IEEE Transaction on Systems, Man and Cybernetics*, 1, 62-66.
22. Russ J (2002) *The Image Processing Handbook*, CRC Press, Boca Raton, Florida.
23. Beucher S and Lantéjoul C (1979) Use of watersheds in contour detection. *Proceedings of International Workshop Image Process, CCETT, Rennes, France*.

24. Hangartner TN (1987) Correction of scatter in computer tomography images of bone. *Medical Physics*, 14(3), 335-340.
25. www.ccny.cuny.edu, accessed on 11/7/2008
26. www.statistics.com, accessed on 11/7/2008
27. Thodberg HH and Rosholm A (2003) Application of the active shape model in commercial medical device for bone densitometry. *Image and Vision Computing*, 21, 1155-1161.